The Pennsylvania State University

The Graduate School

Department of Mechanical Engineering

FILM-COOLED GAS TURBINE VANE TEMPERATURE CALCULATIONS WITH AN ITERATIVE CONJUGATE HEAT TRANSFER APPROACH USING EMPIRICAL FILM CORRELATIONS

A Thesis in

MECHANICAL ENGINEERING

by

TIMOTHY JENNINGS

Submitted in Partial Fulfillment
of the Requirements
for the Degree of

Master of Science

May 2011

The thesis of Timothy Jennings was reviewed and approved* by the following:

Savas Yavuzkurt
Professor of Mechanical Engineering
Thesis Advisor

Gita Talmage
Professor of Mechanical Engineering

Karen Thole
Head of the Department of Mechanical Engineering Department

*Signatures are on file in the Graduate School

ABSTRACT

The design of gas turbine blades and vanes is a challenging task. The nature of the problem calls for high speed, high temperature, turbulent flows to be predicted accurately. The conventional technique for solving such flows neglects conduction through the blade material and relies on turbulence models to predict the film-cooled flow. This results in errors as large as 14% when predicting the wall temperature for internally cooled turbine blades. A loosely coupled conjugate heat transfer method called Iterative Conjugate Heat Transfer (ICHT) was developed to incorporate conjugate effects. A Reduced-Order Film Model (ROFM) was also developed to use experimental data or empirical correlations in place of turbulence models for solving film-cooled flow.

ROFM automates the process of setting up and solving CFD solutions. The development and a demonstration of this technique is presented. A CFD solution of a film-cooled C3X blade was obtained to determine the influence of conjugate effects and the accuracy of ROFM. Results show a maximum deviation for wall temperatures of 3.33%, which was roughly 2.5% of the initial total gas temperature, and equivalent to 18 °C, showing good agreement with experimental results. The change in wall temperature due to conjugate effects was a maximum of 40 °C, which is considered very significant in gas turbine design.

Table of Contents

List of Figures

List of Tables

Nomenclature

T	=	Temperature, K
U	=	Velocity, $\frac{m}{s}$
h	=	Non-film-cooled Heat Transfer Coefficient, $\frac{W}{m^2K}$
$q^{"}$	=	Surface Heat Flux, $\frac{W}{m^2}$
c_p	=	Specific Heat, $\frac{J}{kgK}$
$\frac{h_f}{h_o}$	=	Heat Transfer Augmentation Due To Film Injection
η	=	Film Effectiveness, Eq. (6)
θ	=	Dimensionless Wall Temperature, Eq. (7)
Pr	=	Prandlt Number
Br	=	Brun Number, Eq. (2)
St	=	Stanton Number
Re	=	Reynolds Number
x	=	x Coordinate
D	=	Hole Diameter
M	=	Blowing Ratio, Eq. (1)
Tu	=	Turbulence Intensity
$\propto$	=	Surface Angle of the Cooling Hole
δ_1	=	Momentum Thickness, m
L	=	Length of the Plate or Airfoil, m
s	=	Lateral Spacing of Cooling Holes, m

Subscripts

o	=	Non-film-cooled; Baseline
f	=	Film-cooled
G	=	Free Stream Gas
F	=	Film
C	=	Coolant
W	=	Wall
R	=	Recovery
AW	=	Adiabatic Wall
M	=	Metal
$conj$	=	Conjugate Parameter
$non-conj$	=	Non-conjugate Parameter

Accents

$\bar{X}$	=	Average Quantity

Acknowledgments

I would like to thank my family first. My parents have always been supportive of furthering my education and it is nice to know that they are proud of what I've accomplished. They've always been ready and willing to offer a helping hand, and I feel grateful and lucky to have them.

I would also like to thank Pratt & Whitney for funding the research project and providing me with a job after I graduate. The work environment I discovered there is rather close to my version of a dream job so I'm very excited to get started. I'd also like to thank some of the people who work at Pratt. Dr. Kohli got my foot in the door, always gave great advice and was good for a laugh. Dr. Bradshaw and Dr. Martin were always there to bounce ideas or engage in excellent lunch conversations. I'm looking forward to more in the future.

I've met some amazing teachers in my college career. The most noteworthy among them were Dr. Talmage at Penn State, Dr. Zitarelli at Temple and Dr. Peridier at Temple. These three strike me as having the best classroom manner I've ever seen. I always looked forward to going to their classes.

Dr. Yavuzkurt, my thesis advisor, was instrumental in helping me throughout my time on the project. Even graduate students gossip, and I believe that I was lucky in finding a phenomenal advisor that works because he loves the topic and truly puts his students first. Thank you very much for your help.

I'd also like to thank my friends. A good laugh does more for keeping a person sane than anything else I can think of and they provided plenty of laughs.

Saving the best for last, I would like to thank my fiancée Clare. God only knows how she put up with two years of me being at school. Clare is a fantastic woman. She was always ready to offer support by hanging out while I studied or did work, or simply saying she was sure I could do it, regardless of what "it" was. She is the rare type of person that pushes you to your goals and to improve yourself. She is a challenge and a puzzle I think I'll never manage to figure out. Clare is a large part of the reason I've been able to make it to where I am today. For all of that and much more, I love her.

Chapter 1: Introduction

1.1 Background

Airlines and air framers continue to push gas turbine technology in hopes of improving efficiency, increasing thrust specific fuel consumption and lowering weight. For the power output of an engine to double, the rotor inlet temperature would have to increase from 2500 to 3500 F [1]. At such elevated temperatures, multiple modes of structural failure are present include creep, cracking, oxidation, and melting. Keeping the metal components from failing in the turbine requires constant cooling. There are various cooling technologies that allow the blades to operate in temperatures hundreds of degrees above their melting temperatures. The most common techniques used today are convection cooling, impingement cooling and film-cooling. A general sense of the expected temperature range for a given technology is shown in Figure 1.

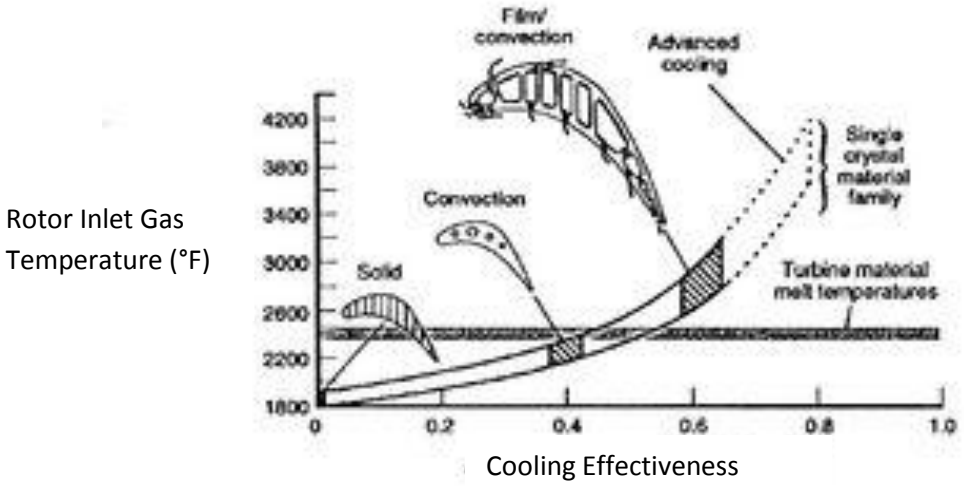

Figure 1: Pictures of Film-Cooling Technology with Graph of Effectiveness [2]

Convection cooling refers to bleeding air from the compressor stage and passing it through cavities in the blade material. The cooling air is fed through the root of the blade. Often times turbulators, or "trip strips", are used to enhance mixing and increase the heat transfer in serpentine channels passing through the blade, such as in Figure 2. Convection cooling is very common, and is often combined with other cooling techniques, such as impingement or film-cooling.

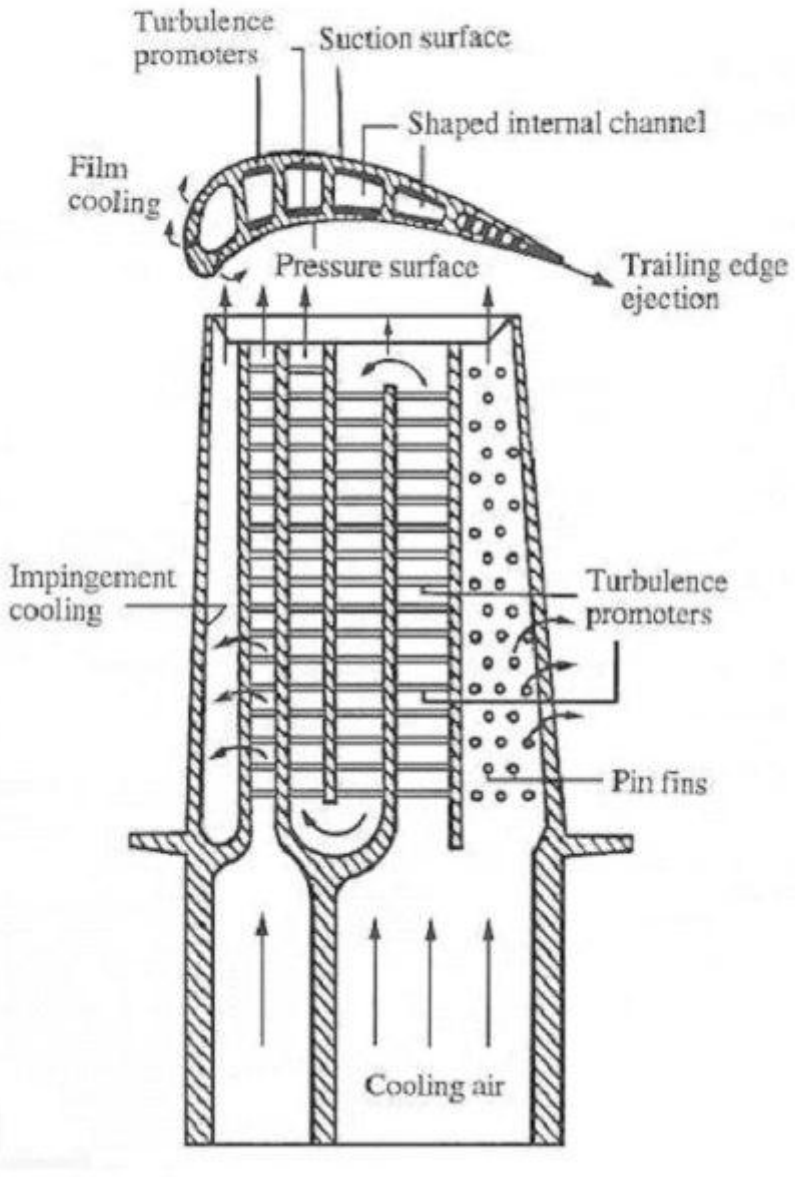

Figure 2: Schematic of Typical Film-Cooling Design [3]

Impingement cooling refers to cooling the back side of shell airfoil by directing jets. The shell is fabricated like sheet metal and offset from the rest of the blade material. Figure 2 shows impingement cooling at the leading edge of the blade. This method of cooling is very effective and is often utilized on early stage blades and vanes, where temperatures of the gas stream are the highest, in combination with other cooling schemes.

Film-cooling refers to jets of coolant air that are injected into the boundary layer through discrete holes in the blade. This cooling technique is very effective and provides protection by using the

coolant air to displace the hot exhaust gases and insulate the blade material from excessive heat transfer. Oftentimes, film-cooling is used in concert with other cooling techniques. It is not uncommon for the cooling jets to be fed from a convective cooling serpentine or for discrete cooling holes to be drilled into the shell of an impingement cooled airfoil.

The focus of this paper will be flows with film-cooling. The purpose of this study is to further the development and validation of a model for performing film-cooling calculations while including the thermal resistance of the metal, known as conjugate heat transfer effects.

1.2 Experimental Studies on Film-Cooling

Goldstein [4] summarized various geometry and flow related effects on film-cooling flows. Ekkad et al. [5] published a study measuring effectiveness and heat transfer data using transient liquid crystallography. They showed how utilizing a compound injection angle can increase film effectiveness. The study was performed on a flat plate. Baldauf et al. [6-9] gathered film effectiveness and heat transfer augmentation data for various blowing ratios and injection angles. The data was later put into the form of empirical correlations. Yuen & Martinez-Botas [10-13] published round hole effectiveness and augmentation data with various array configurations. Both authors provided span-wise averaged and two-dimensional contour plots of their data sets. Gritsch et al. [14-15] performed high speed experiments with diffuser holes on a flat plate. Data was reported for Mach numbers up to 0.6 and blowing ratios up to 2.0. The blowing ratio is defined by Eq. (1).

$$M = \frac{\rho_C U_C}{\rho_G U_G} \tag{1}$$

All of the studies mentioned reported non-conjugate results. Hylton et al. [16-17] performed high speed, high temperature studies on a C3X vane in a linear cascade. The blade material chosen was stainless steel, allowing for conduction effects to play a prominent role in heat transfer and resulting in conjugate data. The data reported in this study is much more representative of what occurs in an engine as a result. Both experimental data and numerical results were reported in this study.

1.3 Numerical Studies on Film-Cooling

There are many numerical studies available for film-cooling. The numerical prediction of film-cooled flows with reasonable results is limited to the recovery region. Yavuzkurt & Habte [18] reported that Reynolds Averaged Navier-Stokes (RANS) models under predict mixing in the near field resulting in higher film effectiveness values. RANS models varied in their results, but ranged from under predicting effectiveness by as much as 80% to over predicting by as much as 200%. The best performance was by the epsilon model, which stayed around 20% error for its effectiveness prediction. Figure 3 is a plot of these results. It can be seen that predicted values do not become reasonable until x/D > 3. The location x/D > 3 represents the exit region of the near field of the injection site and entrance into the wake region. Azzi and Lakehal [19] showed that RANS models under predict lateral spreading of the film. The result of such studies is that RANS models are inadequate in the near field. This currently holds true for all turbulence models. Figure 4 is of a typical film-cooling geometry for a first stage blade likely to be seen in a high temperature gas turbine. Turbulence models would be very unreliable for predicting such

a flow because by the time one film jet leaves the near field and settles down in the wake region, the solution enters the near field of the next cooling hole. It should also be noted that a first stage vane would have even more film-cooling holes on the airfoil surface than shown in Figure 4 as it is a half stage closer to the combustor outlet which would cause larger discrepancies in predictions of film effectiveness and heat transfer augmentation for film-cooled flows solved using turbulence models.

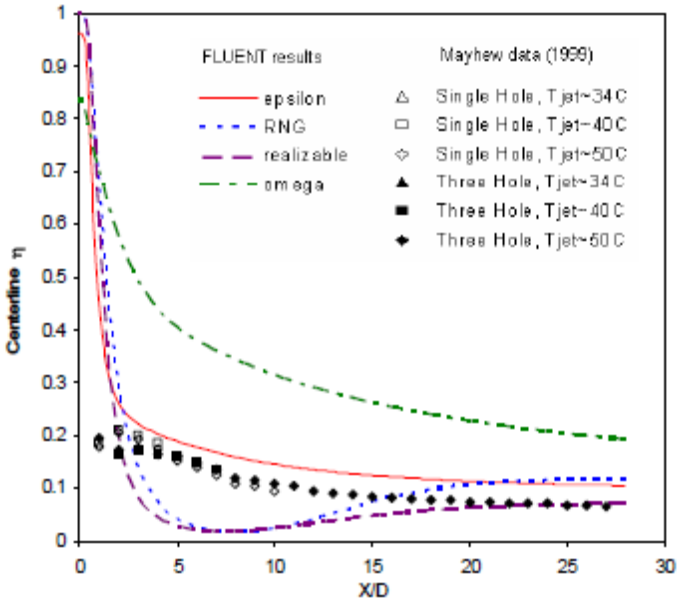

Figure 3: Numerical Prediction of Film-Cooling Effectiveness Using Fluent Compared with Experimental Data [18]

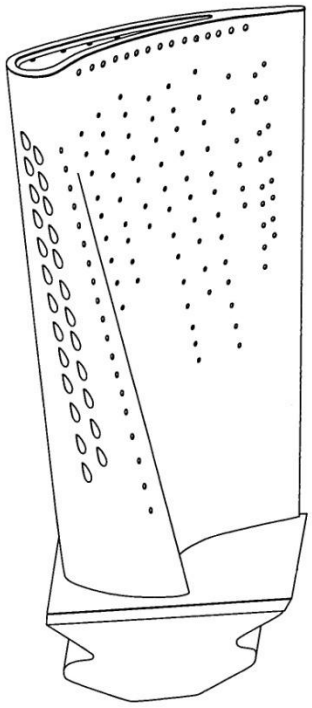

Figure 4: Typical Film-Cooling Configuration for a First Stage Blade [20]

1.4 Conjugate Film-Cooling Studies

Metal conduction through the blade material is also important when determining correct wall temperature values for a blade. Silieti et al. [21] showed that conjugate heat transfer models have significantly improved temperature prediction results. They found that a full conjugate solution couples fluid flow and heat transfer, providing a significant improvement in near field effectiveness results. Bohn et al. [22] reported an 8% difference in temperature results for conjugate and non-conjugate solutions for a film-cooled blade.

1.5 Conclusions

The literature shows multiple gaps in the predictive capabilities of conventional Computational Fluid Dynamics (CFD) programs for film-cooled flows. Turbulence models are incapable of providing satisfactory results in the near field, making them unacceptable for predicting wall temperatures for early stage turbine vanes and blades. Turbulence models have fallen behind experimental findings. An alternative method for solving near-field film-cooled flows is needed. Further, any film-cooled airfoil should be solved in a manner that includes blade conduction in the solution, successfully resolving conjugate effects. Given the low thermal conductivity of the blade material and thermal barrier coatings, such effects can have a large influence on the final wall temperature value predicted. Reports with conjugate and non-conjugate data are necessary for a complete understanding of the problem, but cannot be readily found. An additional complication is that although there have been numerous studies performed, many experimental studies do not include sufficient data on film effectiveness, heat transfer augmentation or geometries.

1.6 Objectives of Research Project

The main objective of this study is to develop a conjugate heat transfer model called the Reduced-Order Film Model (ROFM) which replaces turbulence models with experimental data or empirical correlations for solving the film-cooling flow phenomena. To achieve this objective, the following must be accomplished:

- Validate the Reduced Order Film Model and a proprietary empirical film-cooling model using Hylton et al. [16] experimental data. The author reported conjugate wall temperatures, allowing the method to be benchmarked.
- Increase the accuracy of ROFM through with addition of local reference temperatures. Currently a constant reference temperature from the inlet is used. The temperature of the free stream gas changes significantly as it goes past the airfoil. Including local variation is important for developing the model to solve flows with work extraction and is a necessary step for preparing ROFM as a design tool.
- Expansion of ROFM to include treatment of two-dimensional data, allowing for three-dimensional blade temperature distributions by mapping surface boundary conditions instead of span wise averaged boundary conditions. This is necessary for solving the complex three-dimensional airfoil shapes currently employed by the industry.
- Expansion of ROFM to the near field to be able to apply it to full coverage film-cooled blades. Accurately solving the near field in film-cooling flows is crucial to improving the design of early stage vanes and blades.
- Report on temperature variation between conjugate and non-conjugate solution approaches for the Hylton case [16]. A better understanding of the changes associated with a conjugate solution for an airfoil in a gas turbine engine is necessary and this a step towards that goal.

Chapter 2: Conjugate Heat Transfer Theory

2.1 Physical Explanation of the Difference between Conjugate and Non-Conjugate Approaches

Understanding the difference between conjugate and non-conjugate solutions is easier with diagrams. Figure 5 is a diagram of both solution approaches. The non-conjugate approach places the heat flux at the interface between the metal and the fluid. This is done because a non-conjugate solution assumes that the metal is negligible. This would result in a constant temperature distribution throughout the solid. The conjugate solution approach places the heat flux below the metal to allow for conduction resistance to influence the temperature distribution.

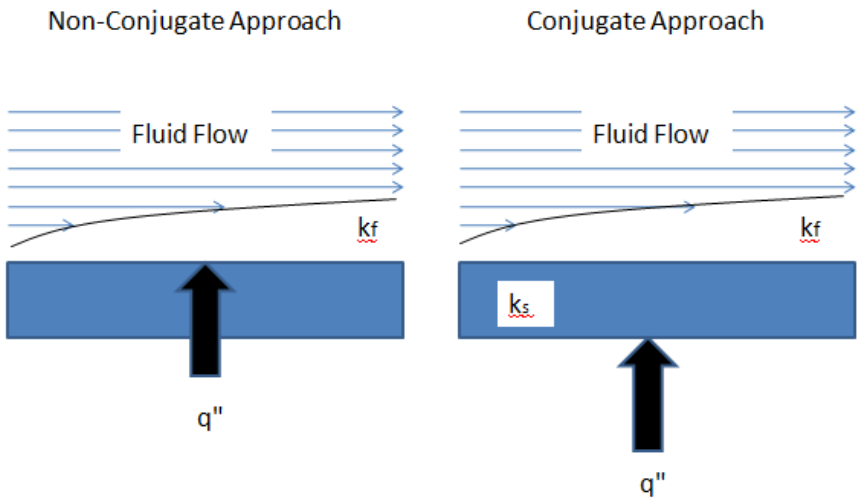

Figure 5: Heat Flux Placement for Conjugate and Non-Conjugate Solutions

Figure 6 shows the difference between non-conjugate and conjugate solutions. The non-conjugate solution has a constant metal temperature since there is no thermal resistance through the metal surface. The gas temperature varies from the metal temperature to the free stream value through the boundary layer, creating a gradient. The conjugate solution has a variable temperature through the metal due to thermal resistance. Here, the temperature rises from the metal temperature, T_M, to some interface temperature T_I. The gas temperature varies from the interface temperature to the free stream value through the boundary layer, creating a different gradient than seen in the non-conjugate case.

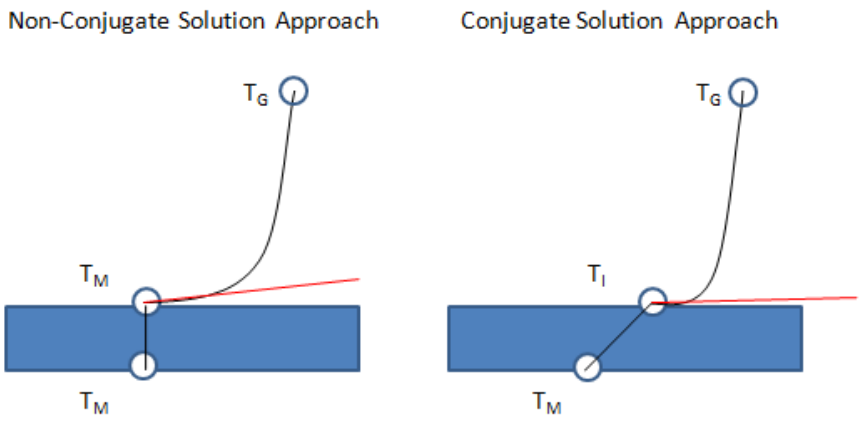

Figure 6: Temperature Assignment and Gradients for Conjugate and Non-Conjugate Solutions

Comparing the gradients of the non-conjugate and conjugate cases, shown in Figure 7, reveals that the slope of non-conjugate gradient is not as large. This is caused by the higher temperature at the interface. The difference between these two approaches is that the inclusion of thermal resistance for the solid forces the interface temperature to change. The interface temperature T_I causes the gradient and corresponding heat flux at the surface to change. Whether or not this change in the gradient is significant depends on the relative importance of the thermal resistance of the solid to that of the flow.

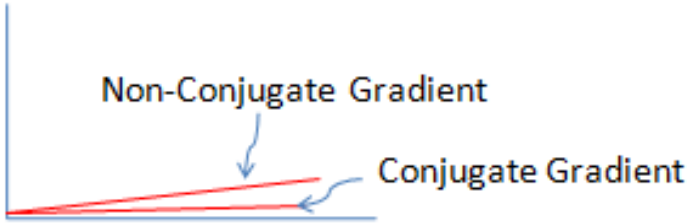

Figure 7: Gradient Comparison for Non-Conjugate and Conjugate Cases

2.2 The Brun Number

The Brun number is a dimensionless parameter that provides a measure of the relative importance of thermal resistances in a problem with a gas flowing over a surface. It can be thought of as a ratio of the thermal resistances of the gas in the boundary layer to the wall over a given length, x, of the surface. This determines whether the resistance of the plate must be considered in order to arrive at an accurate solution. In general, a Brun number over 0.1 requires a conjugate solution. The Brun number definition is given by Eq. (2). The parameters used in Eq. (2) are illustrated in Figure 8.

$$Br_x = \frac{k_f}{k_s}\frac{t}{x}Pr^m Re_x^n \tag{2}$$

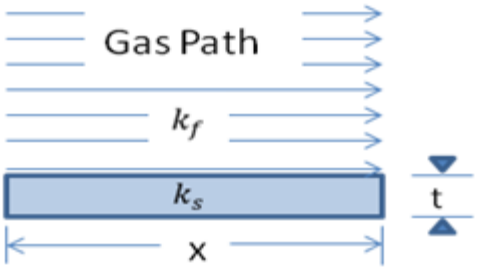

Figure 8: Geometry Example for Brun Number Variable Definitions

The Brun number for the Hylton case [16] is approximately 5.86, well above the 0.1 threshold that requires a conjugate solution. Such high Brun numbers are typical of gas turbine flows.

2.3 Benefits and Limitations of Full Conjugate Analyses

Full conjugate analyses allow for the user to easily define the problem. This is because the interface boundary condition is to force the same heat flux for both domains. Using this condition is especially helpful because it is not possible to accurately specify the wall temperature prior to solving the flow field, which depends in part on the wall temperature. This frees the user to define any external boundary conditions necessary, such as free stream gas temperatures and pressures, and avoid having to enforce a value at the interface. Here, all the temperatures are solved for. As a result, full conjugate analyses are useful for any problem that can be resolved satisfactorily using available turbulence models. A consequence of this dependence is that whenever turbulence models are inaccurate, full conjugate analyses are unreliable. Film-cooling flows are such a case.

Turbulence models are incapable of accurately predicting the flow field near injection sites, termed the near field. Predictions are better after the near field, in the recovery region, however this limits the applicability of conventional CFD. The first vane in a turbine is an example of a problem that turbulence models are incapable of solving accurately. The solid is exposed to extremely high gas temperatures, upwards of 3200 °F for military applications, and is covered with film-cooling holes. Were a turbulence model to be applied to such a problem the results would be inaccurate because the entirety of the blade is near field. This is termed full coverage film-cooling. At present, full conjugate analyses are currently incapable of generating an accurate prediction for such a problem. As a result of these limitations, this method was not used for calculating film-cooled flows.

2.4 Benefits and Limitations of Loosely Coupled Conjugate Analyses

Loosely Coupled Conjugate methods employ mapping of boundary conditions to allow the user to separate the two computational domains at the interface, in this case the airfoil and the gas region. CFD is used to solve the flow field around the profile of the airfoil and heat transfer coefficients are obtained based on a chosen initial temperature. These values are mapped as an external boundary condition imposed on the airfoil, along with any internal boundary conditions necessary to fully define the problem, and the second computational domain is solved. This allows for a wall temperature to be determined. Further, these results ignore any secondary effects associated with the conduction resistance of the blade and thermal barrier coatings. These are not yet conjugate results. To incorporate

conjugate effects requires iterating until the wall temperature converges, while enforcing continuity of heat flux between the two computational domains. This allows for the domains to interact despite being calculated separately.

A loosely coupled conjugate analysis was chosen for calculating film-cooled flows because it meets the requirements for flexibility needed in the model. Using a loosely coupled method allows for the heat transfer coefficients to be modified prior to being mapped onto the solid surface. This modification can be based on empirical film-cooling models or experimental data. This ability to modify values in-between solving domains is a requirement for ROFM.

2.5 Development of Iterative Conjugate Heat Transfer Method

Developing ICHT was rather straightforward. The design required loosely coupled conjugate heat transfer to be automated in a CFD package. ANSYS' Fluent was ideal for this project for multiple reasons. The program is capable of understanding Scheme, a programming language, and allows for various calculations or macros to control a solution through text based commands. Fluent is also capable of executing Unix and Linux command line prompts, allowing for other programs to be called by the Scheme code while running Fluent. In this case, the desired program is MATLAB, which allows for the mapping of boundary conditions as well as any transformations that may become necessary. MATLAB can also be used to check if the interface temperature has converged and stop Fluent from executing further iterations. A graphical overview of the process in shown in Figure 9 and a flow chart of the process is shown in Figure 10.

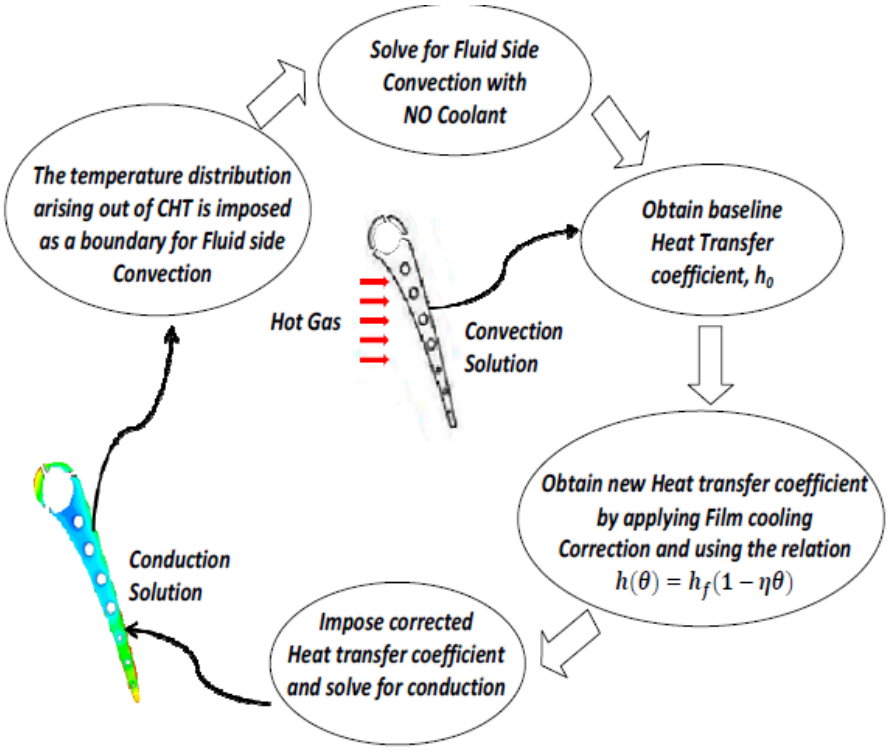

Figure 9: Graphical Representation of ICHT and ROFM[23]

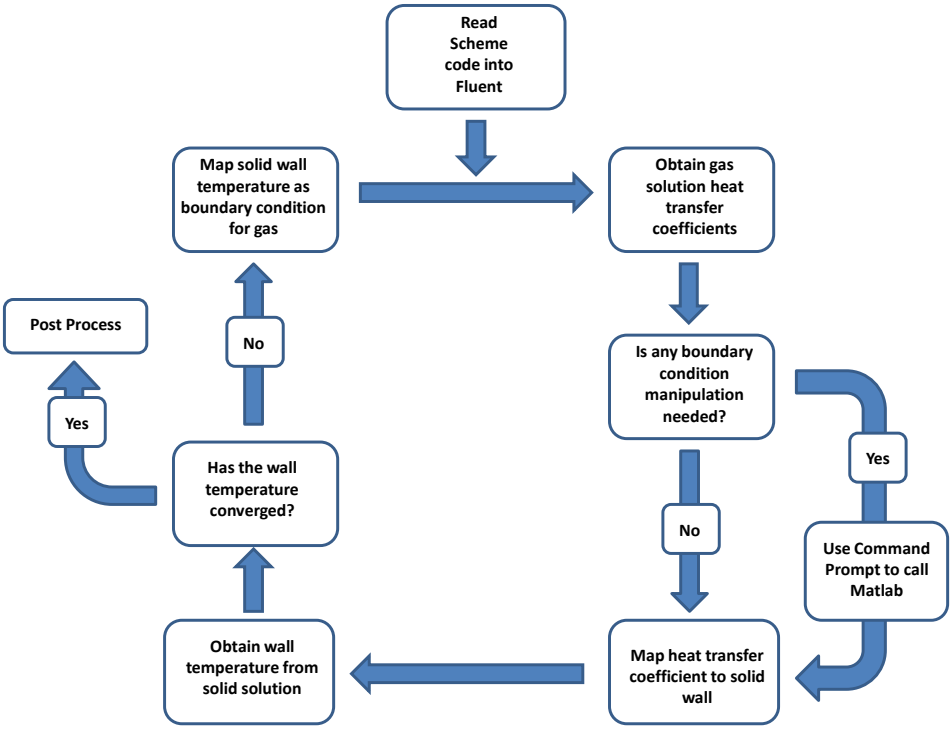

Figure 10: ICHT Flow Chart Showing Matlab Controls

Validation of the method was completed by Dhiman [24]. Luikov [25] published an analytical solution to laminar flow over a flat plate with Br = 1.91. The problem was modeled and solved in Fluent using ICHT. ICHT results, shown in Figure 11, were in good agreement with approximately 1% deviation from the analytical solution.

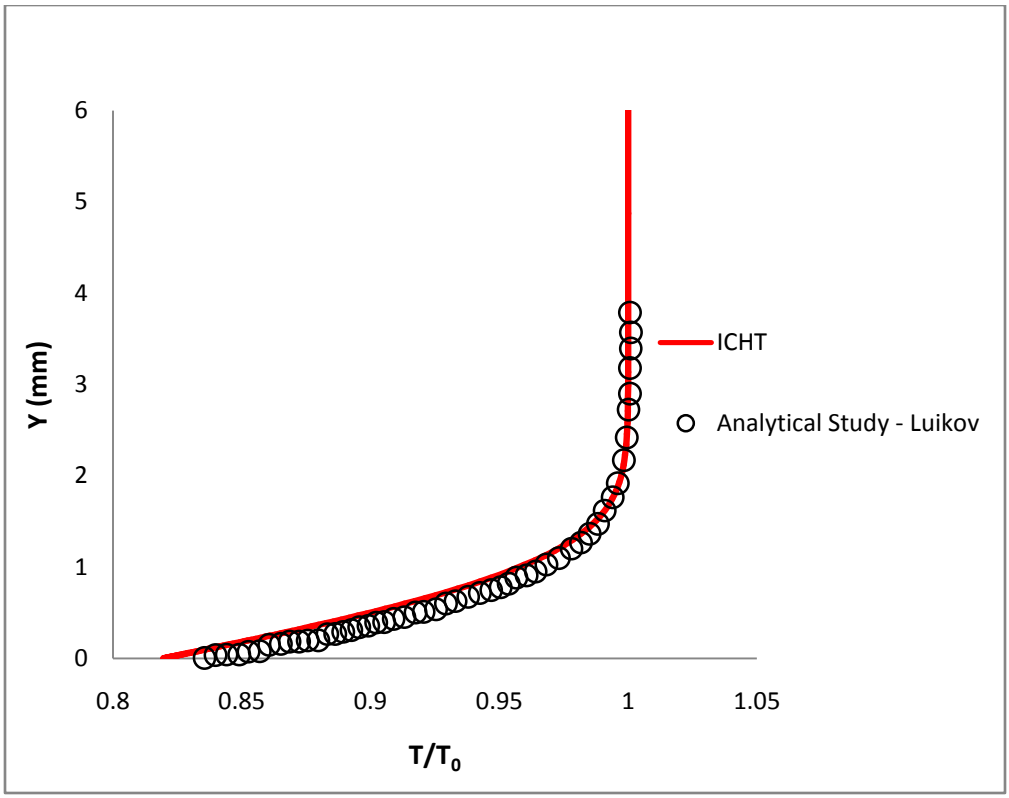

Figure 11: ICHT Results Compared to Conjugate Analytical Solution [23,24]

Chapter 3: Film-Cooling Theory

3.1 Derivation of Important Film-Cooling Parameters

Dimensionless parameters are often desired for studying fluid mechanics and heat transfer. Film-cooling flows are no exception. Deriving the dimensionless film-cooling parameters requires a definition of the heat flux to the surface with and without the presence of a film and those heat fluxes are given below:

$$q_f^{"} = h_f\,(T_G - T_W) \tag{3}$$

$$q_o^{"} = h_o\,(T_F - T_W) \tag{4}$$

The film temperature, T_F, is defined as the temperature after the injected coolant mixes with fluids in the boundary layer. This is shown in Figure 12.

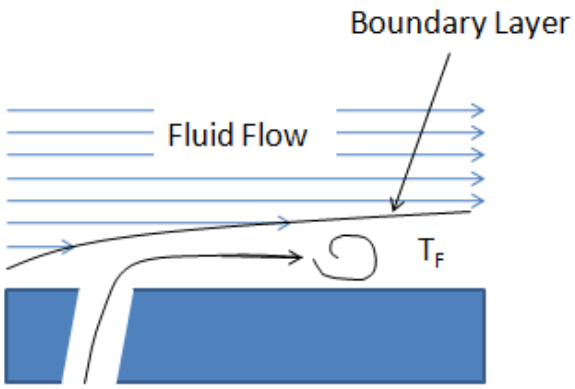

Figure 12: Injection of Film and Definition of the Film Temperature

A dimensionless quantity can be defined by taking the ratio of these quantities.

$$\frac{q_f^{"}}{q_o^{"}} = \frac{h_f\,(T_F - T_W)}{h_o\,(T_G - T_W)} \tag{5}$$

After some minor manipulations, the standard parameters used in analyzing film-cooled problems can be derived from Eq. (5):

$$\frac{q_f^{"}}{q_o^{"}} = \frac{h_f}{h_o}\,\frac{(T_F - T_W + T_G - T_G)}{(T_G - T_W)}$$

$$\frac{q_f^{"}}{q_o^{"}} = \frac{h_f}{h_o}\left[\frac{T_G - T_W}{T_G - T_W} - \frac{T_G - T_F}{T_G - T_W}\right] * \left[\frac{T_G - T_C}{T_G - T_C}\right]$$

$$\frac{q_f^{"}}{q_o^{"}} = \frac{h_f}{h_o}\left[1 - \left(\frac{T_G - T_F}{T_G - T_C}\right)\left(\frac{T_G - T_C}{T_G - T_W}\right)\right]$$

$$\frac{q_f^{"}}{q_o^{"}} = \frac{h_f}{h_o}\left[1 - \eta\theta\right] \tag{6}$$

$$\eta = \frac{T_G - T_F}{T_G - T_C} \tag{7}$$

$$\theta = \frac{T_G - T_C}{T_G - T_W} \tag{8}$$

Consider the terms that appear in Eq. (6). The heat transfer augmentation term, h_f/h_o, is important. This parameter indicates that it is possible for film-cooling to cause a net heat flux increase to the surface. Injecting coolant into the flow results in a large amount of turbulence production and enhanced mixing. The boundary layer energy level is disturbed and as a result heat transfer coefficients change from what would be observed in the case without film-cooling. It is possible for a reduction or increase in the heat flux, although generally the value increases in design problems because of the need to avoid backflow. Based on this, the domain for the augmentation term would be, $0 < h_f/h_o < \infty$. For practical purposes $1 \leq h_f/h_o \leq 2$ should be expected.

Equally important is the film-effectiveness parameter, η, defined in Eq. (7). This provides a method for analyzing how much protection is being provided by gauging how close the film temperature is to the coolant temperature. Generally at an injection site it is possible for this value to be one. As the effectiveness decays due to mixing with the free stream gas, the decrease in the protection provided by the film is seen in a corresponding decrease in η. For any film-cooled problem, $0 \leq \eta \leq 1$.

The last term is the dimensionless wall temperature, θ, defined in Eq. (8). This value gives a sense of what the surface temperature is with respect to the coolant temperature. It should be noted that if the film effectiveness at an injection site is 1, then the dimensionless wall temperature is as well. For cases with no internal cooling, it is not possible for the wall temperature to go below the temperature of the coolant at the injection site, so $1 \leq \theta < \infty$. For cases with internal cooling this condition is no longer valid, so $0 < \theta < \infty$. A high θ value can occur towards the trailing edge of the airfoil. While it is possible that this is caused by an error in the problem setup, the product $\eta\theta$ should be used to determine if this is the case. If $\eta\theta > 1$, and θ is high, then there is an error present in the problem setup.

It is important to note that in design problems, the only value that would be considered constant is the coolant temperature at the inlet to the blade, T_C. In any film-cooled problem h_f/h_o, η, θ, T_W, and T_F are all functions of space. In many problems, such as in gas turbines, the gas temperature, T_G, is also a function of space. If a more complex analysis were necessary for resolving trailing edge wakes or gas migration, these variables would also be a function of time.

3.2 Development of Reduced-Order Film Model

ICHT was designed as a loosely coupled solution method to allow for incorporating ROFM. By combining both models, the final temperature results represent both film-cooling and conjugate heat transfer effects. This requires combining the change in heat flux associated with film-cooling with those caused by conjugate effects. The change in heat flux associated with film-cooling, as derived above, is not quite as useful in this regard. Instead, both effects are considered to be modifiers of a baseline heat transfer value, chosen to be the non-conjugate, non-film-cooled heat transfer coefficient. Let h_θ be defined as a film-cooled, conjugate heat transfer coefficient:

$$h_\theta\left(T_G - T_{W,conj}\right) = h_{f,conj}\left(T_F - T_{W,conj}\right) = q_f^{"} \tag{9}$$

$$h_\theta = h_{f,conj}\left(\frac{T_F - T_{W,conj}}{T_G - T_{W,conj}}\right)$$

$$h_\theta = h_{f,conj}\left(1 - \eta\theta_{conj}\right) \tag{10}$$

The problem is that most experimental film-cooling data does not account for conjugate effects. Typically the metal used in the apparatus is copper, which has a very high thermal conductivity. The reason for using copper is that it allows the researchers to ignore conduction through the metal. For this model to be useful, a method has to be found for converting between conjugate and non-conjugate heat transfer coefficients. The transformation assumed for this research is that the heat transfer augmentation for conjugate and non-conjugate cases will be the same.

$$\left(\frac{h_f}{h_o}\right)_{conj} = \left(\frac{h_f}{h_o}\right)_{non-conj} \tag{11}$$

This assumption is based on film-cooling parameters being solely dependent on the flow field, an assumption already made in the literature. Baldauf et al. [6] define the Stanton number for a film-cooled flow as in Eq. 12.

$$\overline{St}_{f,non-conj} = f\left(\bar{\theta}, M, P, Tu, \frac{x}{D}, \propto, \frac{s}{D}, \frac{\delta_1}{D}, \frac{L}{D}\right) \tag{12}$$

The temperature dependence of in Eq. (12) is not of particular interest, because it limits the range of applicability of the values. Dividing the film-cooled Stanton number by the non-film-cooled Stanton number removes the temperature dependence while preserving the effects of geometry and injection parameters. The temperature dependence is divided out because the non-film-cooled Stanton number is only dependent on the temperature effects.

$$\frac{\overline{St}_{f,non-conj}}{St_{o,non-conj}} = \frac{\overline{h}_{f,non-conj}}{h_{o,non-conj}} = f\left(M, P, Tu, \frac{x}{D}, \propto, \frac{s}{D}, \frac{\delta_1}{D}, \frac{L}{D}\right) \tag{13}$$

Given that the temperature dependence associated with the heat transfer coefficient can be divided for a non-conjugate case, the same assumption should hold for a conjugate solution.

$$\frac{\overline{St}_{f,conj}}{St_{o,conj}} = \frac{\overline{h}_{f,conj}}{h_{o,conj}} = f\left(M, P, Tu, \frac{x}{D}, \propto, \frac{s}{D}, \frac{\delta_1}{D}, \frac{L}{D}\right) \tag{14}$$

Further, since temperature dependence has been removed from the augmentation functions, it makes sense that that the values would be equal for conjugate and non-conjugate analyses as there are no changes to the film-cooling geometry or fluid injection properties. This leads to Eq. (11). Solving for the film-cooled, conjugate heat transfer coefficient yields,

$$h_{f,conj} = h_{o,conj}\left(\frac{h_f}{h_o}\right)_{non-conj} \tag{15}$$

Substituing Eq. (15) into Eq. (10),

$$h_\theta = h_{o,conj}\left(\frac{h_f}{h_o}\right)_{non-conj}(1-\eta\theta) \tag{16}$$

Equation (16) determines the film-cooled, conjugate heat transfer coefficient. The non-film-cooled, conjugate heat transfer coefficient is augmented using empirical or experimental values for heat transfer augmentation and film-effectiveness. The non-film-cooled, conjugate heat transfer coefficient and θ are found through the output of ICHT. This modified heat transfer coefficient is used as the external boundary condition for the solid solution. As a result, film-cooled physics replaces a turbulence model for solving the near field flow.

It is worth noting that it is currently not possible to prove Eq. (11). Doing so would require a data set reporting conjugate and non-conjugate data for film-cooled and non-film-cooled conditions on the same experimental rig. This data set does not exist. It is possible that the augmentation terms are not entirely independent of the temperature, however, it is likely that any temperature dependence is a second order effect.

Now that the model has been defined, some physical understanding of what is occurring is necessary. Substituting the definition for the heat transfer coefficients in terms of heat flux and temperatures into Eq. (10) gives,

$$\left[\frac{q_f^{"}/(T_F - T_W)}{q_o^{"}/(T_G - T_W)}\right]_{conj} = \left[\frac{q_f^{"}/(T_F - T_W)}{q_o^{"}/(T_G - T_W)}\right]_{non-conj}$$

$$\left(\frac{q_f^{"}}{q_o^{"}}\right)_{conj} = \left(\frac{q_f^{"}}{q_o^{"}}\right)_{non-conj}\left(\frac{T_G - T_W}{T_F - T_W}\right)_{non-conj}\left(\frac{T_F - T_W}{T_G - T_W}\right)_{conj}$$

$$\left(\frac{q_f^{"}}{q_o^{"}}\right)_{conj} = \left(\frac{q_f^{"}}{q_o^{"}}\right)_{non-conj}\left[\frac{(T_G - T_W)_{non-conj}}{(T_G - T_W)_{conj}}\right]\left[\frac{(T_F - T_W)_{conj}}{(T_F - T_W)_{non-conj}}\right] \tag{17}$$

Depending on the location, the wall temperature of an airfoil could increase or decrease due to conduction through the metal being considered. Conduction through the metal would reduce the effects of internal cooling. Many airfoils have thermal barrier coatings with very low thermal conductivities. This

would reduce external heating. It is unknown if the temperature will increase or decrease at any given point, however the change can be modeled as an unknown function.

$$T_{w,conj} = T_{w,non-conj} + c_1(x,z) \tag{18}$$

In gas turbine engines, it is known that $T_G > T_F$, however both are functions are space. At the surface,

$$T_G = T_F + c_2(x,z) \tag{19}$$

Substituting Eq. (18) and (19) into Eq. (17) transforms to non-conjugate temperatures and the defined constants,

$$\left(\frac{q_f^{"}}{q_o^{"}}\right)_{conj} = \left(\frac{q_f^{"}}{q_o^{"}}\right)_{non-conj} \left[\frac{T_G - T_W}{T_G - (T_W + c_1)} \frac{(T_G - c_2) - (T_W + c_1)}{(T_G - c_2) - T_W}\right]_{non-conj}$$

$$\left(\frac{q_f^{"}}{q_o^{"}}\right)_{conj} = \left(\frac{q_f^{"}}{q_o^{"}}\right)_{non-conj} \left[\frac{(T_G - T_W)}{(T_G - T_W) - c_1} \frac{(T_G - T_W) - (c_1 + c_2)}{(T_G - T_W) - c_2}\right]_{non-conj}$$

$$\left(\frac{q_f^{"}}{q_o^{"}}\right)_{conj} = \left(\frac{q_f^{"}}{q_o^{"}}\right)_{non-conj} \left[\frac{(T_G - T_W)^2 - (c_1 + c_2)(T_G - T_W)}{(T_G - T_W)^2 - (c_1 + c_2)(T_G - T_W) + c_1 c_2}\right]_{non-conj} \tag{20}$$

$$\left(\frac{q_f^{"}}{q_o^{"}}\right)_{conj} = \varphi\left(T_G, T_F, T_{W,conj}, T_{W,non-conj}\right)\left(\frac{q_f^{"}}{q_o^{"}}\right)_{non-conj} \tag{21}$$

While heat fluxes are temperature dependent, in this non-dimensional form it can be seen that a large amount of the dependency is removed. A functional form has been found for the change in heat flux due to film cooling in conjugate and non-conjugate solutions. For the heat fluxes to be the same, $\varphi = 1$ or $c_1 c_2 = 0$ in Eq. (20). To determining whether or not this makes sense involves examining the constants more closely.

1. $c_1 = 0; T_{w,conj} - T_{w,nonconj} = 0$

   This would be realistic in the event that the metal had a very high thermal conductivity, such as copper. Gas turbine airfoils are made from low thermal conductivity metals protected by low thermal conductivity coatings. A high thermal conductivity assumption is not valid for this problem.

2. $c_2 = 0; T_G - T_F = 0$

   This is valid where there is no film-cooling, and consequently is not very useful for a film-cooling model. It is possible for there to be regions without film-cooling on late stage vanes and blades, but this would likely not occur on first stage vanes and blades, which often have full coverage film-cooling.

For a full coverage blade, it can be seen from Eq. (21) that the heat flux will change due to film-cooling and conjugate effects. Without allowing for the internal resistance of the metal to be accounted for these effects would be neglected, and it is possible for there to be too little or too much cooling. Too little cooling could result in blade failure or shorter part life. Too much cooling results in lower turbine efficiency or less thrust. Both cases are undesirable.

Chapter 4: ROFM Analysis of an Airfoil in a Cascade

4.1 Description of Experiment

The experiment chosen for validation of ROFM was performed by Hylton et al. [16]. It involves an airfoil cascade and includes film-cooled and non-film-cooled test runs. All cases have internal cooling. The metal used, 310 stainless steel, has a low thermal conductivity which allows conjugate effects to be resolved in the experiment. The C3X vane used in the experiment, shown in Figure 13, was chosen as the test airfoil. The vane was cut in-between the film-cooling cavities and the internal cooling holes, numbers one and eleven on the suction side and four and nineteen on the pressure side in Figure 13. The vane was welded back together with a 0.254 mm air gap while maintaining the profile to avoid disturbing the flow path. The gap was intended to act as a thermal barrier, isolating the effects of film-cooling on the surface from the influences of the injection site and feed cavities. In Figure 13, numbers one through ten refer to internal cooling holes, and numbers eleven through nineteen to film-cooling holes. For this study, holes thirteen through seventeen were not considered.

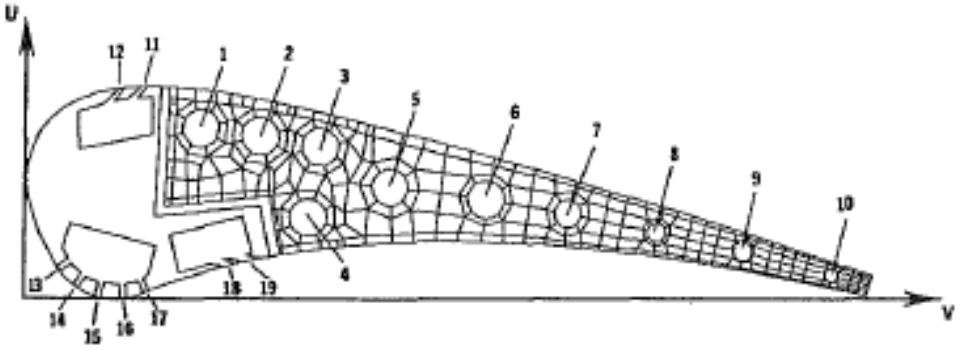

Figure 13: Geometry of Film-Cooled C3X Airfoil [16]

Hylton et al. [16] provided much of the necessary data for generating a model of their modified C3X blade. The exact position of the thermal barrier and internal boundary conditions were not included in the final report. Positioning the thermal barrier was overcome by using a data extraction program to determine its position relative to other geometric points for which positions were given. Using the known values as a reference point, the thermal barrier was properly placed. Once a model of the blade was generated, two meshes were created. The first mesh, shown in Figure 14, used the profile of the blade to create a gas domain to be used for determining external heat transfer coefficients on the airfoil surface. Figure 15 shows a close up of the boundary layer mesh attached to the solid wall and the unstructured mesh used for the bulk of the flow field. The second mesh, shown in Figure 16, is the internally cooled region of the airfoil after the thermal barrier. The leading edge is not of interest for this study because Hylton et al. [16] did not report data for this region. The solid mesh uses the heat transfer coefficients from the flow solution as an external boundary condition and generates wall temperature values that can be compared to the reported measurements. Figure 17 shows a close up of one of the internal cooling holes. A boundary layer mesh was placed around all of the internal cooling holes to properly resolve gradients. An unstructured mesh was used for the bulk of the solid region.

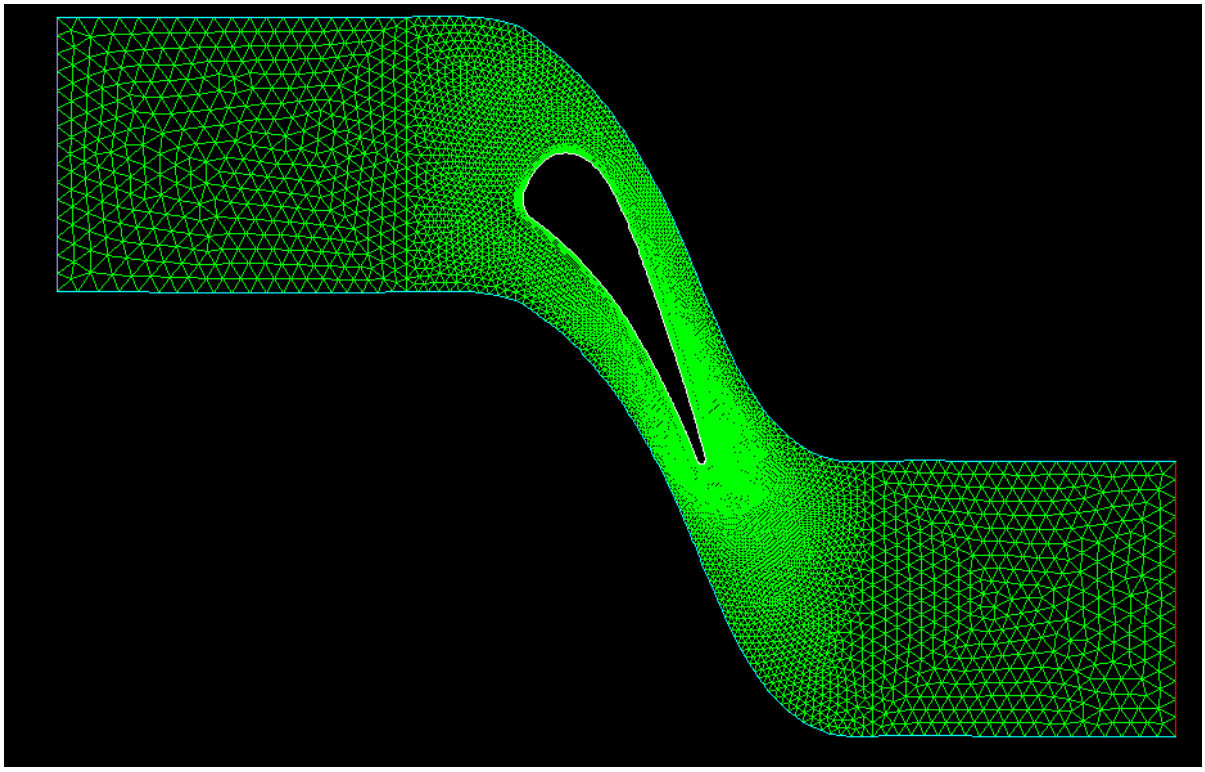

Figure 14: Mesh for Gas Domain For Hylton C3X Blade

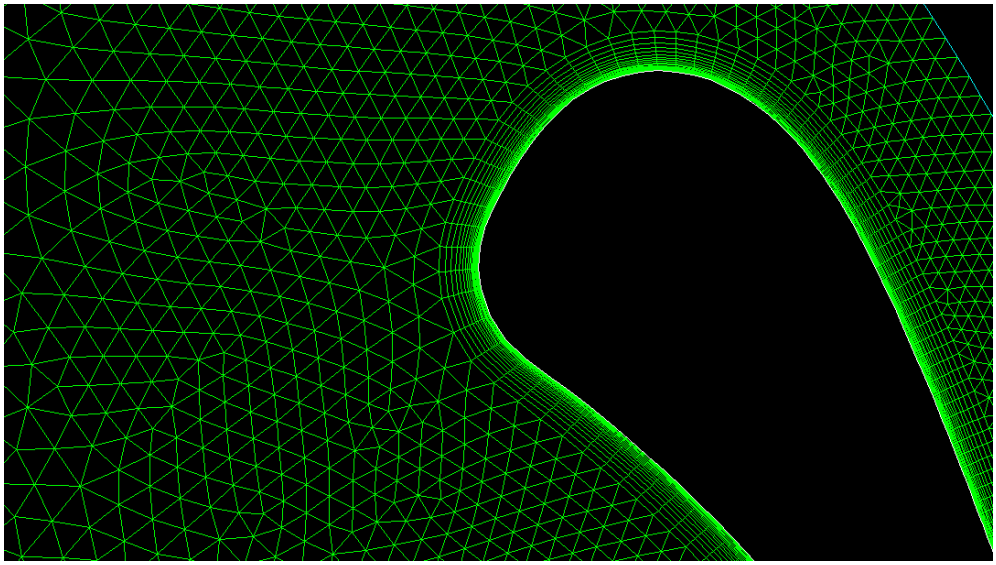

Figure 15: Boundary Layer and Surrounding Unstructured Mesh For Hylton C3X Blade

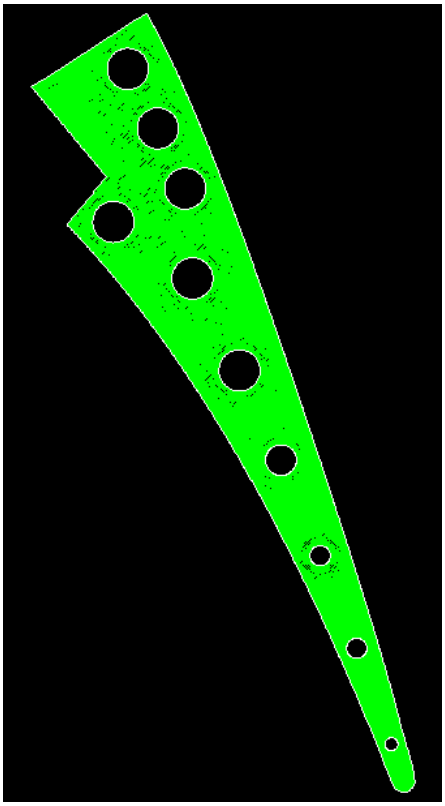

Figure 16: Mesh of Solid Domain For Hylton C3X Blade

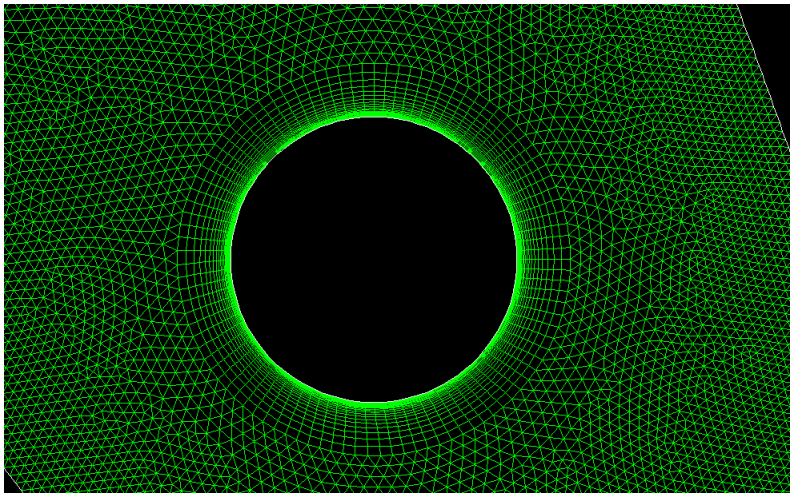

Figure 17: Boundary Layer and Unstructured Mesh Surrounding an Internal Cooling Hole For Hylton C3X Blade

Once the meshes had been established[1], it was decided to use run 44000[2] for validating ICHT on a non-film-cooled case, followed by run 44308 for validating ROFM on a film-cooled case. This solution strategy insures that the physics of the problem have been modeled correctly before adding the

[1] A mesh independence study was performed. Results are provided in Appendix A.

[2] The run numbers refer to specific test cases performed by Hylton et al. [16]. Information of these cases can be found in Appendix B.

additional complication of an empirical film model, effectively narrowing the potential sources of error when comparing the final results to reported experimental data.

4.2 Results of Gas Solution

The first benchmark used with the Hylton case entailed comparing the pressure distribution for the flow solution to experimental data. CFD generally provides good pressure results, especially for two-dimensional solutions. The Hylton case is more complicated than the standard two-dimensional flow because it is transonic which can cause problems in terms of the solution accuracy. The exit mach number for these cases is 0.9, however the peak mach number is 1.04, as shown in Figure 18.

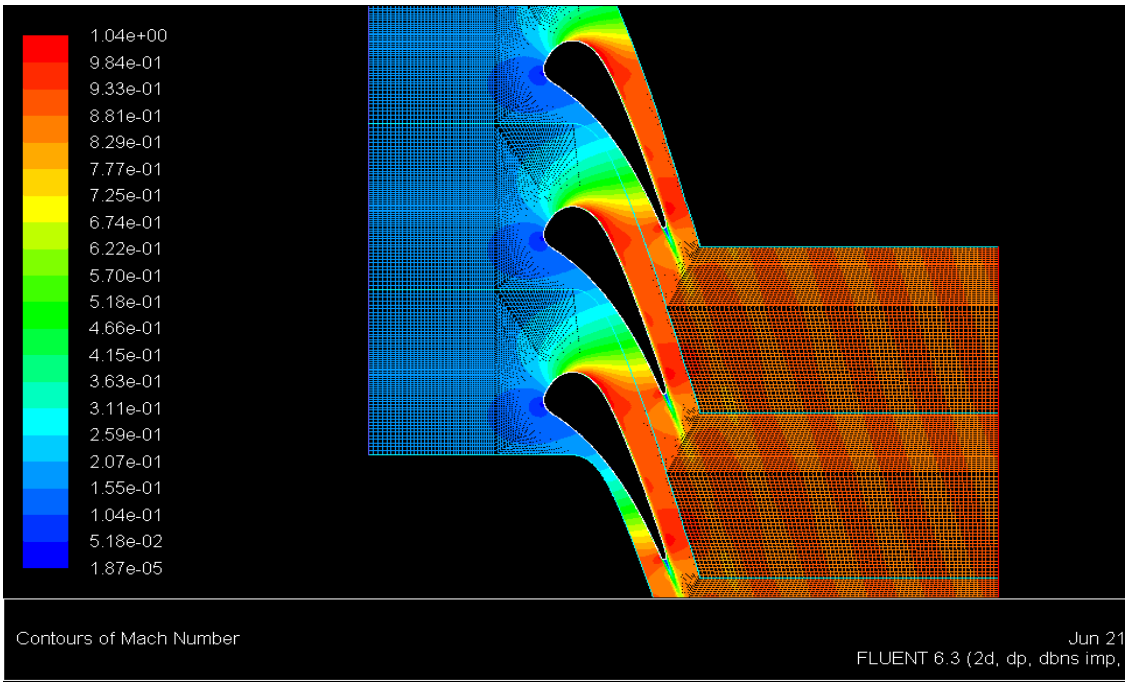

Figure 18: Mach Number Contour For Hylton C3X Blade

High values of the Mach number occur around mid-span and towards the trailing edge of the suction side, as well as the trailing edge of the pressure side. Consider the total pressure, shown in Figure 19, where tail shocks can be identified in the flow leaving the trailing edge of the airfoil and impinging on the suction side at mid-span.

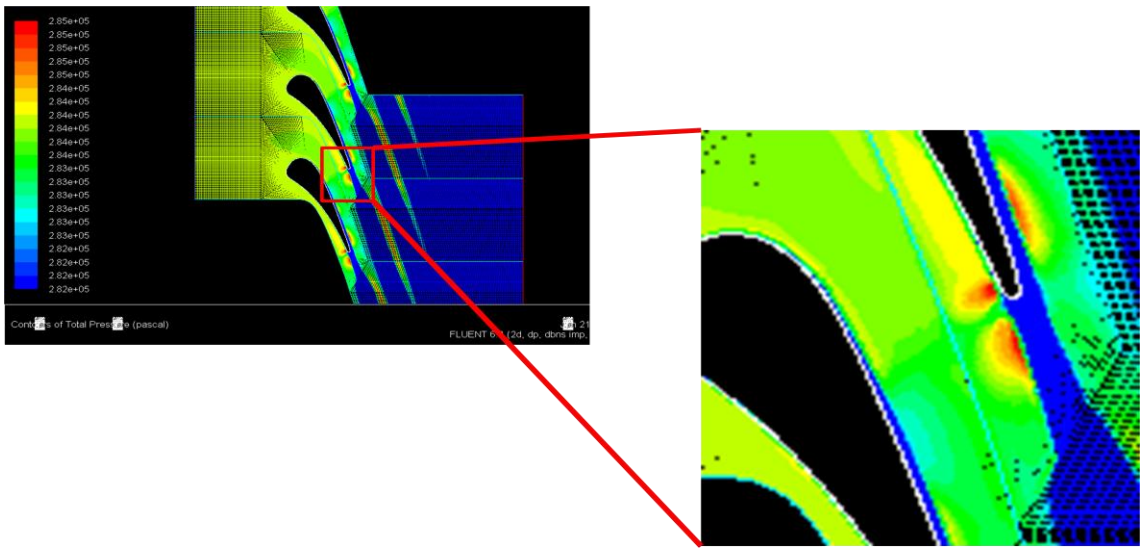

Figure 19: Computed Total Pressure Contour For C3X Blade

Matching the experimental data for the C3X blade was rather problematic. After using two CFD codes, two RANS models, two gas meshes, and two solvers, the experimental pressure distribution data for the case with an exit mach number of 0.9 still could not be met. In an attempt to diagnose the problem, the exit mach number was reduced to 0.75 in an attempt to compare to the second data set measured in the experiment without the potential complication of shocks. Results are shown in Figure 20. The pressure side showed relatively good agreement, but the suction side showed larger than expected deviations, especially around 40% span. Y237 is a proprietary CFD code and V310 an automated meshing program owned by Pratt & Whitney. It should also be noted that the spike at the end of the pressure distribution results is caused by Fluent failing to properly resolve the wake region after the trailing edge of the vane.

Initial trouble shooting involved checking the airfoil geometry, all boundary conditions, and any other user input that could have resulted in an error in the pressure distribution. No problem were found. At this point, the geometry of the airfoil was rotated in an attempt to see if the data points provided by Hylton et al. [16] were slightly skewed. After rotating the airfoil one degree clockwise, improvements were seen in the results for the suction side, however a three degree rotation showed deviations from the data trend. The rotation had no effect on the pressure distribution near the trailing edge of the airfoil. Results are shown in Figure 21.

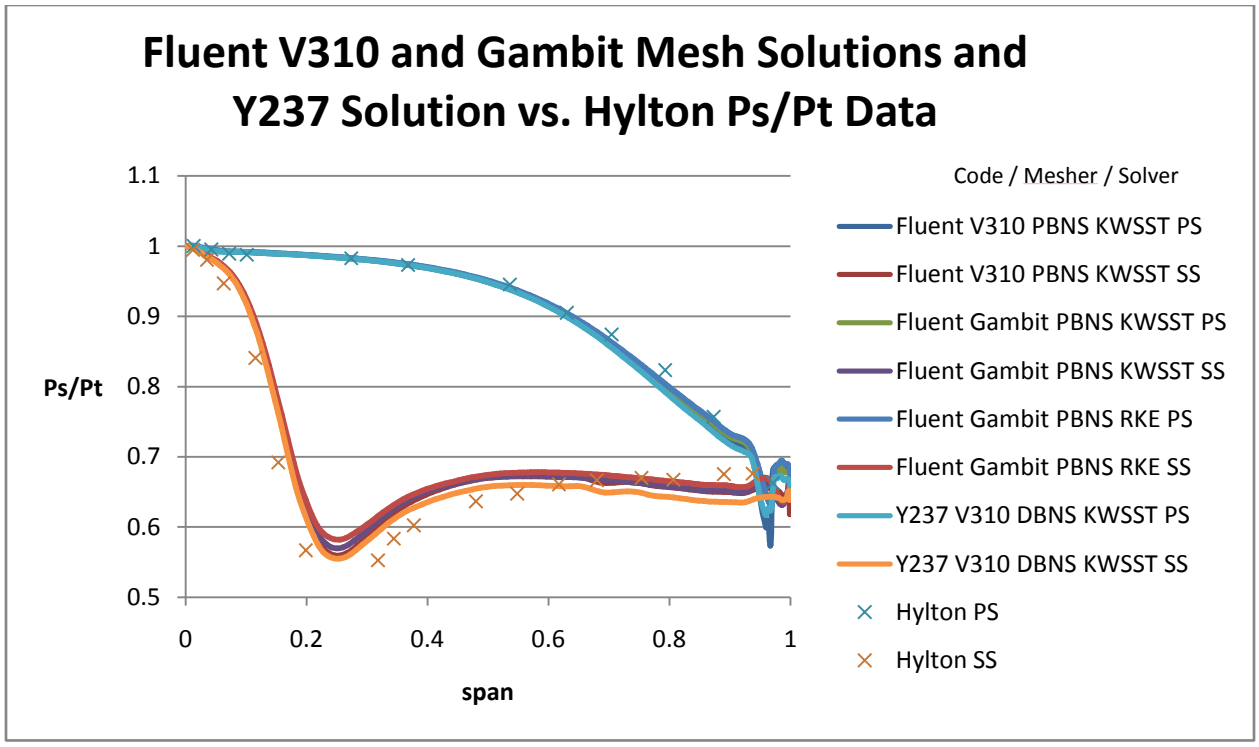

Figure 20: Pressure Distribution for Various Cases vs. Hylton 1988 Data [16]

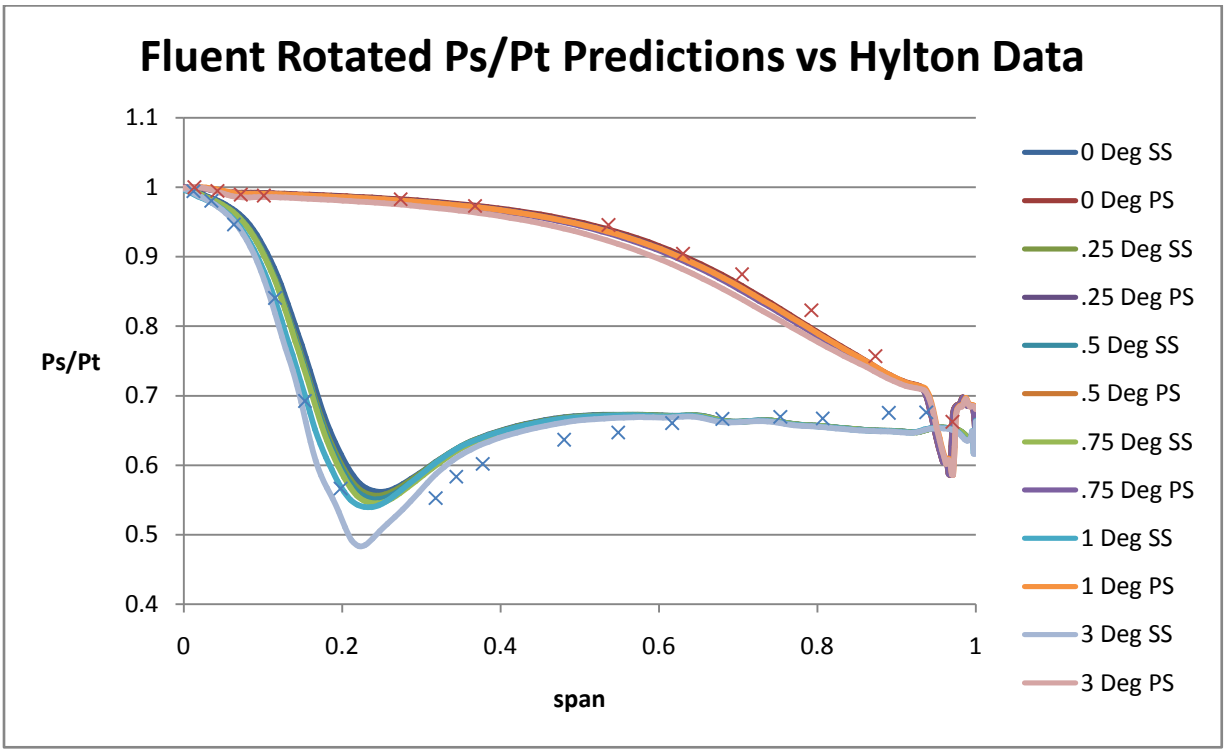

Figure 21: Pressure Results for Rotated C3X Blade vs Hylton 1988 Data [16]

After finding no error in the setup for the case with an exit mach number of .9, results were compared with experimental pressure distribution data from Hylton et al.'s 1983 experiment [17]. The comparison is shown in Figure 22. The suction side showed better agreement with the older data set, although a larger deviation was seen in the pressure side. From this point a brief literature survey found computational results published by Leylek et al. [26] for the Hylton's 1983 [17] C3X blade, shown in Figure 23. Predicted results agreed very well with Leylek's, matching the trend almost identically. It was determined that there was likely some error in the measurement or blade profile reported by Hylton et al. in 1988 [16].

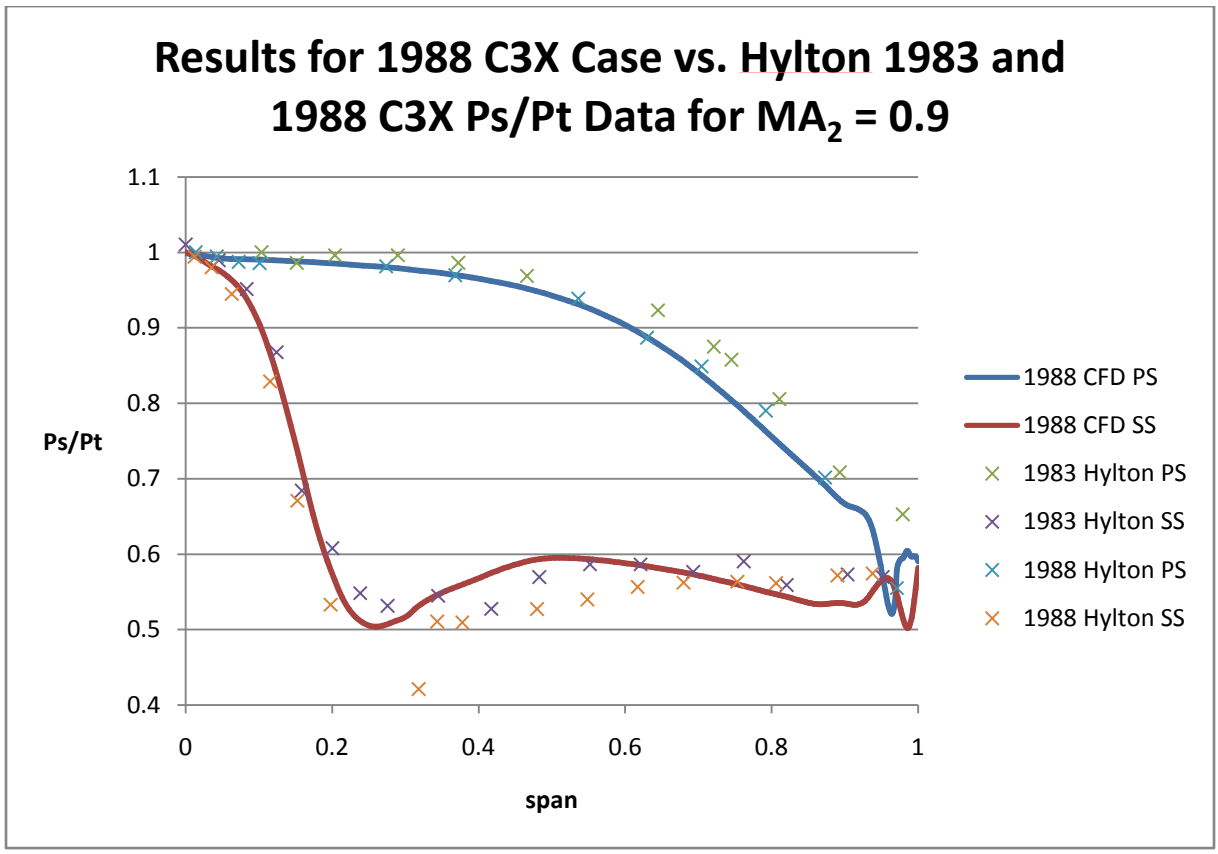

Figure 22: Pressure Distribution vs. Hylton 1983 and 1988 Data [16,17]

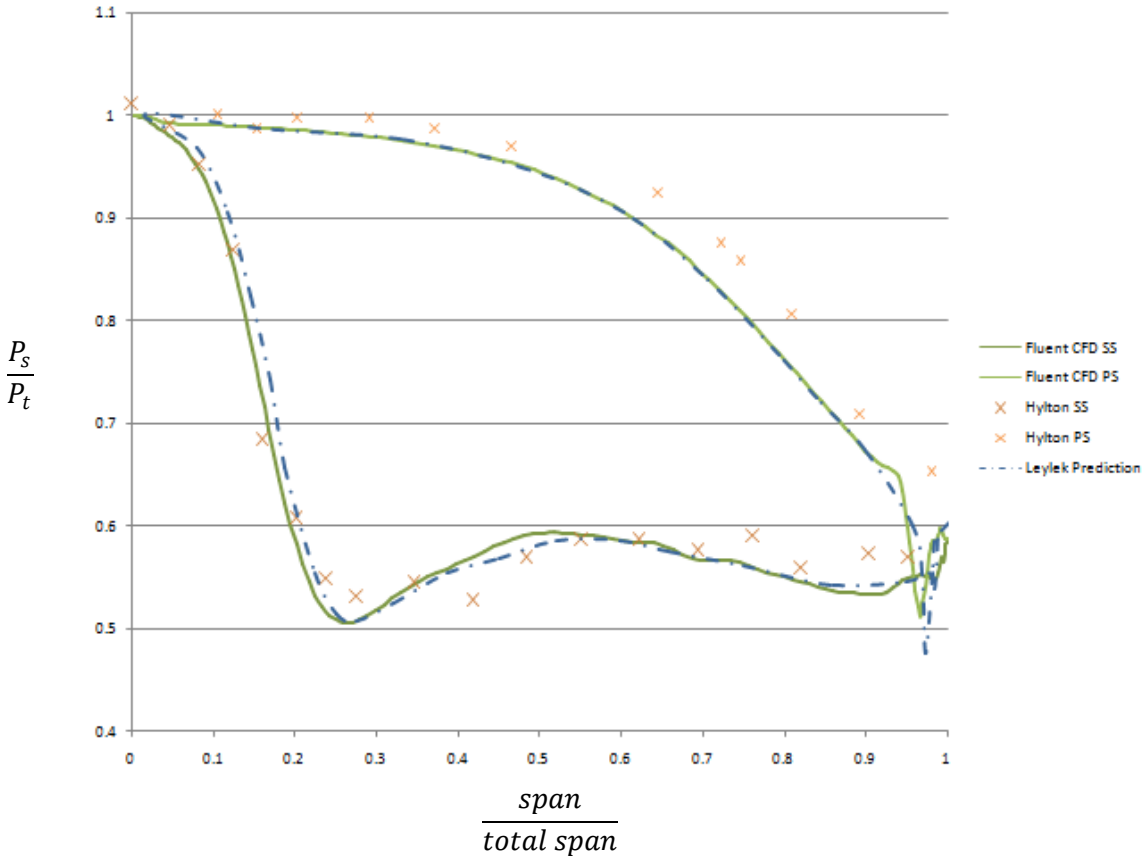

Figure 23: Comparison to Leylek Computational Result for 1983 C3X Blade [26]

4.3 Description of Film Model

Pratt & Whitney, the sponsor of this research project, has an empirical film model used in testing ROFM. The model is designed to predict the initial values and decay of film-cooling effectiveness and local heat transfer augmentation for airfoils. The model is proprietary in nature and so cannot be reported in any detail, however, a prediction of values for the Hylton experiment were generated. Predicted values for the suction side are shown in Figure 24. Values for pressure side are shown in Figure 25. Both figures are plotted against the span of the airfoil. It should be noted that there are two peaks in the heat transfer augmentation and film effectiveness predictions because there are two cooling holes.

The blue line refers to the local heat transfer augmentation. The value is set as one prior to reaching a cooling hole, then increases due to the first injection. This value starts to decay until it reaches the second hole, at which point it increases again. Then the augmentation value decays, eventually reaching its baseline value of one. Local film effectiveness follows the same trend.

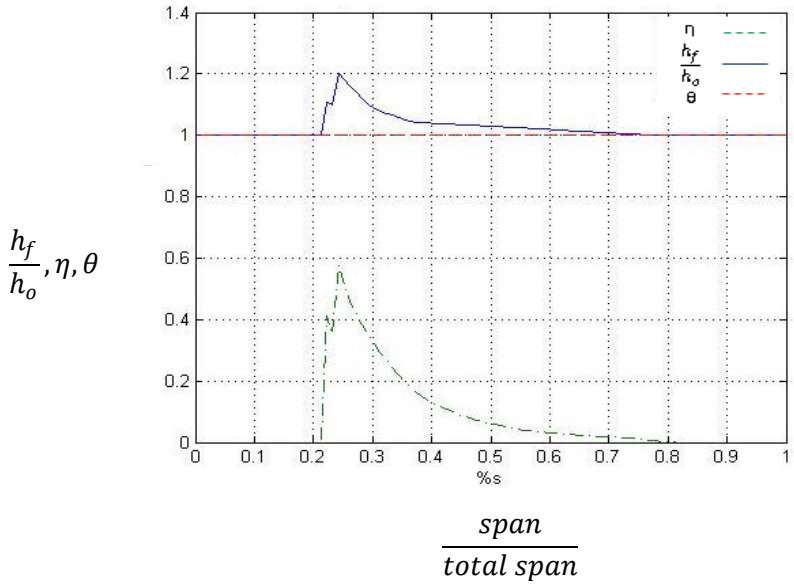

Figure 24: Suction Side Film Effectiveness and Heat Transfer Augmentation

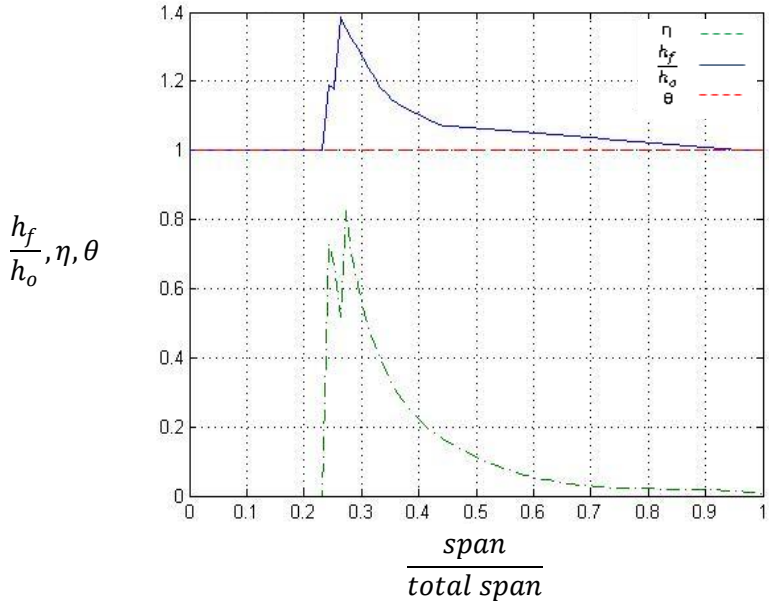

Figure 25: Pressure Side Film Effectiveness and Heat Transfer Augmentation

4.4 Non-Film-Cooled Results

Run 44000 was used for the non-film-cooled case. Hylton et al. [16] neglected to report a large amount of data that would have been useful in determining boundary conditions. This includes thermocouple data taken inside the thermal barrier and the mass flow rates and temperatures for the internal cooling holes. As a result, a the values used in for the boundary conditions had to be found elsewhere or improvised based on an understanding of the physics involved.

The internal boundary conditions were found in a report by Laskowski et al. [27]. An inverse process was used to determine these values based on matching reported data using full conjugate CFD analyses on cases without film cooling, shown in Table 1.

	Final values	
Hole #	$\dot{m}$ (kg/s)	T (K)
1	0.00784	425.25
2	0.00793	367.06
3	0.00794	350.79
4	0.00826	402.94
5	0.00748	325.10
6	0.00691	326.76
7	0.00752	360.59
8	0.00770	422.46
9	0.00473	379.99
10	0.00357	421.32

Table 1: Mass Flow Rate and Inlet Temperature for Hylton C3X Internal Cooling Holes [27]

These values were then used in a full conjugate three dimensional model created and analyzed by Dhiman [24] to arrive at average heat transfer coefficients and bulk temperatures. This was done to create boundary conditions for the internal cooling holes of a two-dimensional model. Results are reported in Table 2.

Hole	*Diameter (m)*	*Cr*	*k (W/m-K)*	*ρ (kg/m³)*	*ν (m²/s)*	*ṁ (kg/s)*	*Re_D*	*Nu_D*	*$\bar{h}$ (W/m²K)*	*T_b (K)*
1	0.0063	1.118	0.03574	0.81875	0.0000297	0.00784	65159.52	143.9797	816.79	431.74
2	0.0063	1.118	0.031872	0.93943	0.0000236	0.00793	72135.19	156.1841	790.14	376.45
3	0.0063	1.118	0.030765	0.97944	0.0000220	0.00794	74231.84	159.8053	780.38	361.13
4	0.0063	1.118	0.034151	0.86515	0.0000271	0.00826	71201.46	154.5646	837.86	408.66
5	0.0063	1.118	0.02908	1.0461	0.0000197	0.00748	73095.61	157.8454	728.59	338.18
6	0.0063	1.118	0.029377	1.03381	0.0000201	0.00691	67206.43	147.5868	688.19	342.20
7	0.0047	1.09	0.031893	0.93872	0.0000236	0.00752	91645.75	184.4138	1251.38	376.74
8	0.0031	1.056	0.036116	0.80853	0.0000303	0.0077	129092.3	234.9965	2737.78	437.18
9	0.0031	1.056	0.036668	0.79372	0.0000312	0.00473	78449.04	157.7652	1866.10	445.32
10	0.00198	1.025	0.037108	0.782231	0.0000320	0.00357	91655.13	173.4309	3250.33	451.83

Table 2: Average Heat Transfer Coefficients and Bulk Temperatures for Internal Cooling Holes [24]

The thermal barrier posed problems as well. The first guess for a boundary conditions was adiabatic, however when the blade profile was restored with the air gap in place, an insulating material was not used. Hylton's report describes welding the blade together, indicating heat transfer would occur across the thermal barrier at the boundaries. Without the temperature data taken from thermocouples along the thermal barrier, it was not possible to impose these values on the solid mesh and use the resulting heat fluxes as a boundary condition. The final boundary condition used was an extrapolated wall temperature at the edge, based on reported values, and an adiabatic condition elsewhere along the thermal barrier.

With approximate values for the missing boundary conditions, it became possible to solve the problem. Because of the boundary conditions are not exact, they are the main source of error in the solution. Results of the first analysis, with these conditions applied, are illustrated in Figure 26.

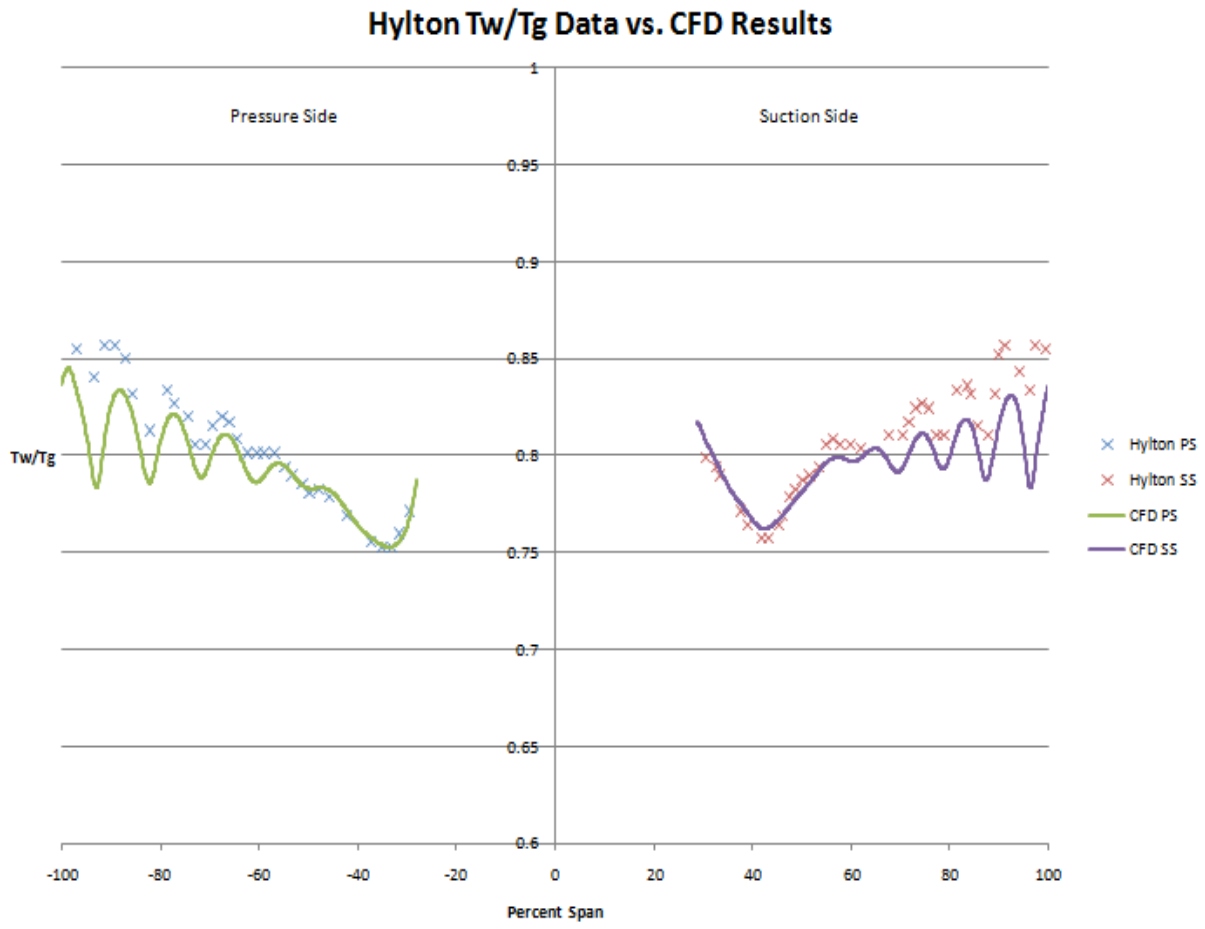

Figure 26: Wall Temperature Results with Initial Internal Cooling Boundary Conditions

Results showed very good agreement in the region directly after the thermal barrier, however the prediction towards the trailing edge of the airfoil was less accurate, showing deviations as large as 6%. The error was associated with the fact that a steady state solution was assumed. The result was that the average heat transfer coefficients were unrealistically high. With the amount of data missing 6%

error is reasonable. While this solution is acceptable, it showed that the boundary conditions needed further iteration. This was necessary because the film-cooled solution is to be used for validation, and any source of error that could be removed from the baseline case does not have to be considered in the film-cooled results. The value of the internal heat transfer coefficients for the last few holes were reduced until the predicted temperature distribution was more accurate. The adjusted values are reported in Table 3.

		Old Values	New Values
Hole	T_b(K)	h (W/m_2K)	h (W/m_2K)
1	431.7	816.79	1002.94
2	376.5	790.14	942.7
3	361.1	780.38	941.47
4	408.7	837.86	1018.64
5	338.2	728.59	849.73
6	342.2	688.19	799.41
7	376.7	1251.38	1100
8	437.2	2737.78	2500
9	445.3	1866.1	1700
10	451.8	3250.33	2000

Table 3: Adjusted Internal Heat Transfer Coefficients

Results from the analysis using the adjusted heat transfer coefficients are shown in Figure 27. Temperature predictions were brought in line with reported experimental data, with deviations reappearing around 85% span. The maximum deviation was reduced from 6% to 2.4%, very close to the 2.0% experimental error reported for the study. The remaining error in the solution is associate with the trailing edge wake. It is not properly resolved, and the internal heat transfer coefficients are directly affected by this phenomena.

Based on the temperature distribution, it is clear that the majority of the physics in the flow are being properly resolved. This can be seen by how well the wall temperature trend matches that of the data, showing that the internal cooling holes and flow are being modeled accurately. The results were in good agreement with experimental data and further refinement of the baseline boundary conditions would be less valuable, so it was decided to move on to the film-cooled case.

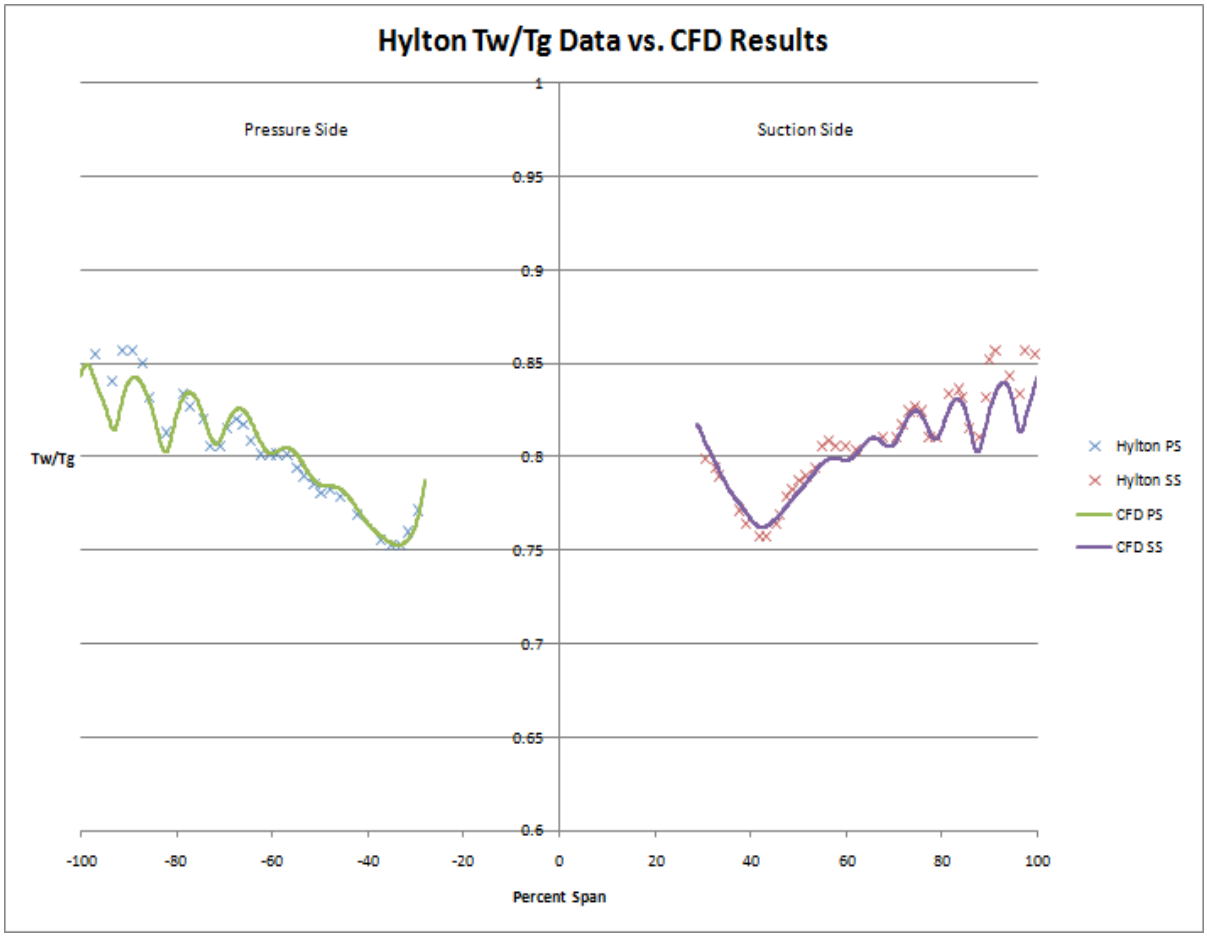

Figure 27: Final Wall Temperature Results for the Non-Film-Cooled Run

4.5 Results for the Film-Cooled C3X Vane

For the case of a modified C3X vane a version of the Matlab script containing decay curves produced from Pratt & Whitney's film-cooling model was used. These curves were specific to the Hylton test case. Given the empirical nature of the model, it is important to check key values to insure that the solution is behaving as expected. Figures 28 and 29 show the product $\eta\theta$ from the first iteration and sixth iteration, respectively. The first iteration plot represents non-conjugate results, whereas the sixth iteration plot has conjugate effects incorporated in the solution. Neither plot shows $\eta\theta$ greater than one, indicating that the solution was well behaved. This product is important in that $\eta\theta$ above one would result in the airfoil heating the external gas, and be a sign that something is wrong.

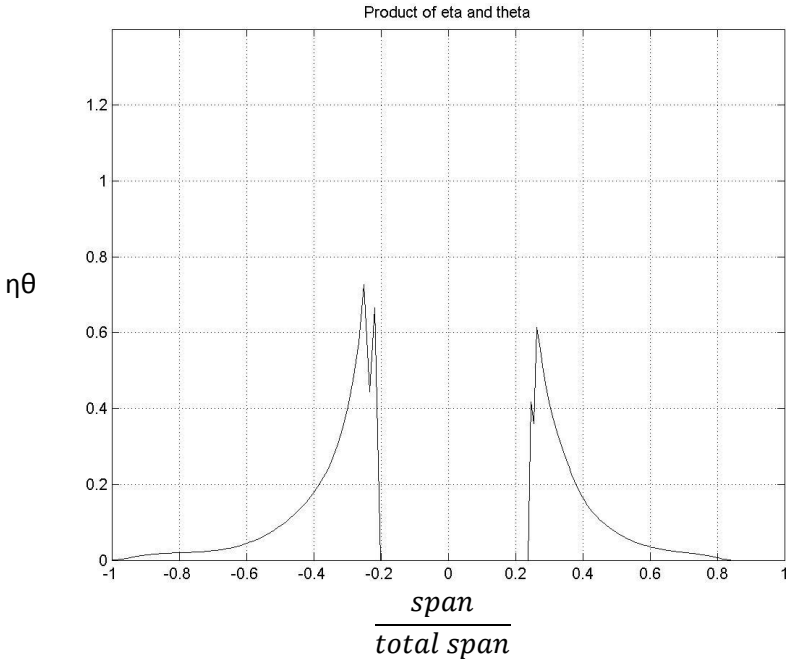

Figure 28: Product of Eta and Theta for Iteration 1 for Film-Cooled C3X Solution

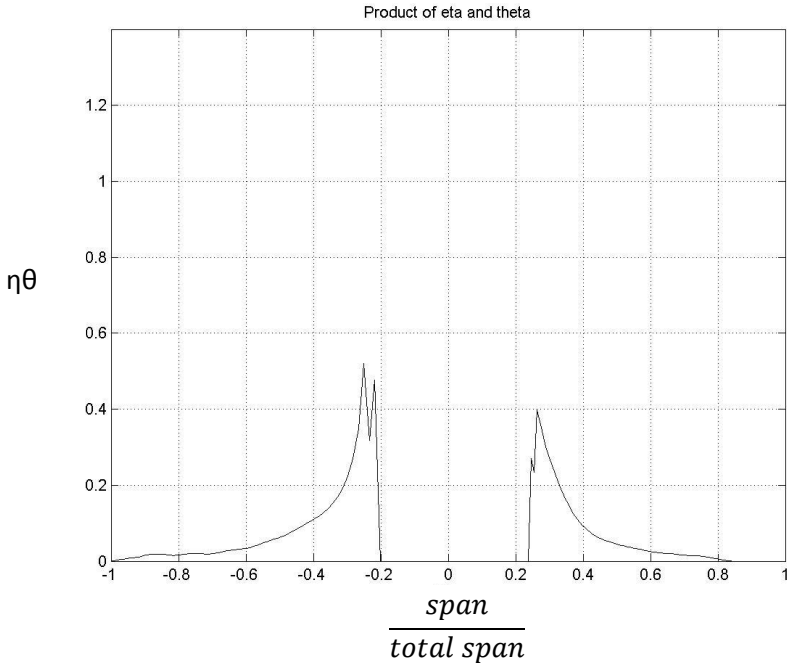

Figure 29: Product of Eta and Theta for Iteration 6 for Film-Cooled C3X Solution

Another gauge for determining whether the solution is physically realistic is to determine whether the assumption made while developing ROFM is reasonable. Consider Eq. (17), which is reproduced here,

$$\left(\frac{q_f^{"}}{q_o^{"}}\right)_{conj} = \left(\frac{q_f^{"}}{q_o^{"}}\right)_{non-conj} \left[\frac{(T_G - T_W)^2 - (c_1 + c_2)(T_G - T_W)}{(T_G - T_W)^2 - (c_1 + c_2)(T_G - T_W) + c_1 c_2}\right]_{non-conj}$$

It is already known that the gas temperature is above the film temperature everywhere in the problem. This means that the function $c_2(x)$ is not of concern. Therefore if $c_1(x) = T_{W,conj} - T_{W,non-conj} \neq 0$ where the model is being applied, i.e. where $\eta > 0$, then a nonzero value means that there is a change in heat flux associated with conjugate effects. This is shown below in Figure 30.

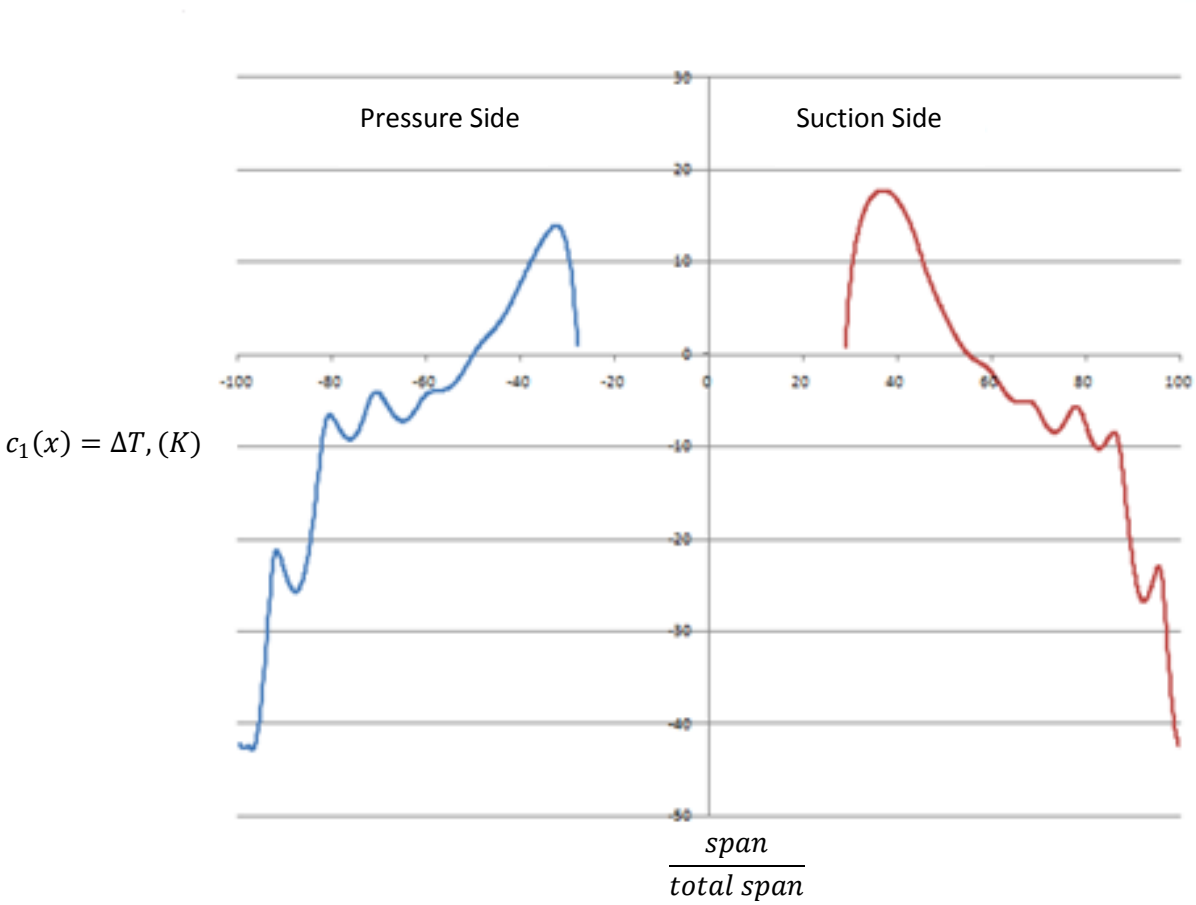

Figure 30: Temperature Difference between Conjugate and Non-conjugate Solutions

Interestingly the value of $c_1(x)$ changes from positive to negative at roughly 50% span for the pressure side and 60% span for the suction side. These likely correspond to the regions where the internal cooling begins to dominate over the effects of film-cooling. From Figure 29, it can be seen that this switch occurs when $\eta\theta$ is less than 0.1, when the film-cooling has largely mixed out. Further, looking at the final temperature distribution in Figure 31, the predicted conjugate and non-conjugate

temperatures were equal at the same location where $c_1(x) = 0$, as expected from the model. All of the important parameters are behaving as expected so the solution is physically relevant.

Despite using entirely empirical values for film-cooling parameters, the predicted wall temperature was within 3.33% of experimental data. The wall temperature measurements performed by Hylton et al. were within $\pm$ 2% experimental error (black lines in Figure 31). If the experimental error associated with the film-model were to be considered in this value, the prediction would likely fall within the expected range. Unfortunately these values are proprietary and were not provided.

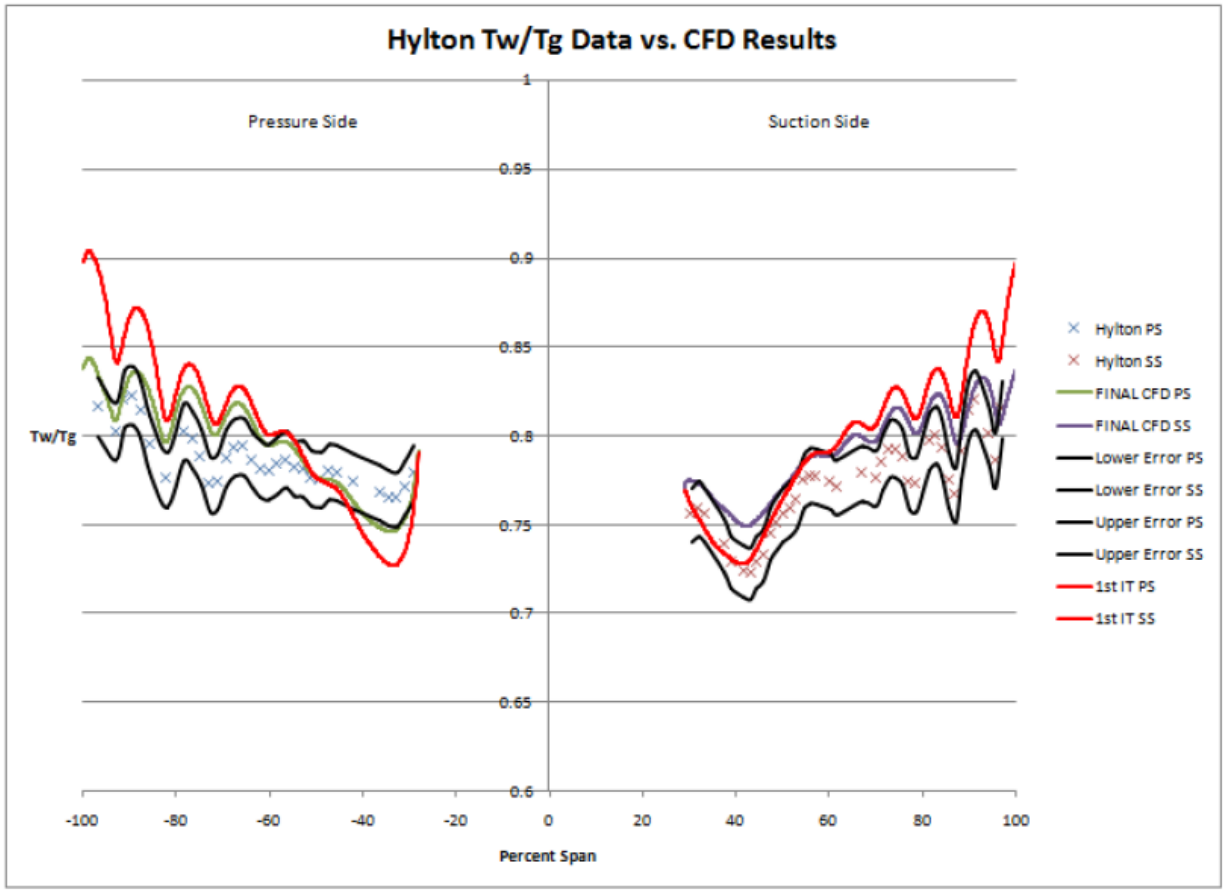

Figure 31: Final Wall Temperature Results for Film-Cooled C3X Vane

These results are sufficiently good to validate both ROFM and Pratt & Whitney's empirical film model, and provides evidence that the underlying assumption for ROFM is reasonable. The slope of the predicted values reasonably match that of the reported data, showing that ROFM is resolving the physics of the problem accurately. The largest deviations occur in the film-cooled region of the vane, and this is likely error that can be associated with the empirical film model. However, 3.33% error for a film-cooled flow is a much better result than could be expected from current turbulence models. This solution also shows the need to use a conjugate approach when solving gas turbine blades and vanes. A temperature difference of 40 K is significant for such a design problem, and could result in part failure.

Chapter 5: Improvements and Modifications to ICHT and ROFM

5.1 Local Reference Temperature

In internal flows such as gas turbine blade passages, the main stream gas temperature changes in the flow direction. In order to enhance the capabilities of ROFM and to better match film-cooling definitions with those at Pratt & Whitney, a local reference temperature was introduced to the θ calculation in place of the inlet total gas temperature. It should be noted that the Hylton et al. case [16] was calculated before and after this change was made, with very little deviation in the results. This was expected as the experiment used a cascade. As a result, no work was extracted from the flow, so the total temperature of the free stream gas remained relatively constant.

The value chosen as the local reference temperature was the recovery temperature, T_R, defined as,

$$T_R(x) = T_G(x) + \frac{[Pr\ (T)]^{1/3}[U_G(T)]^2}{2c_p(T)} \tag{22}$$

Values for the local gas temperature and velocity were taken from the periodic boundary condition imposed in the flow solution, shown in Figure 32. The temperature values were used with curve fits for the Prandtl number and specific heat of air to determine the local recovery temperature. It is important to note that Pratt & Whitney defines their adiabatic wall temperature as the recovery temperature, leading to:

$$T_{AW}(x) = T_R(x)$$

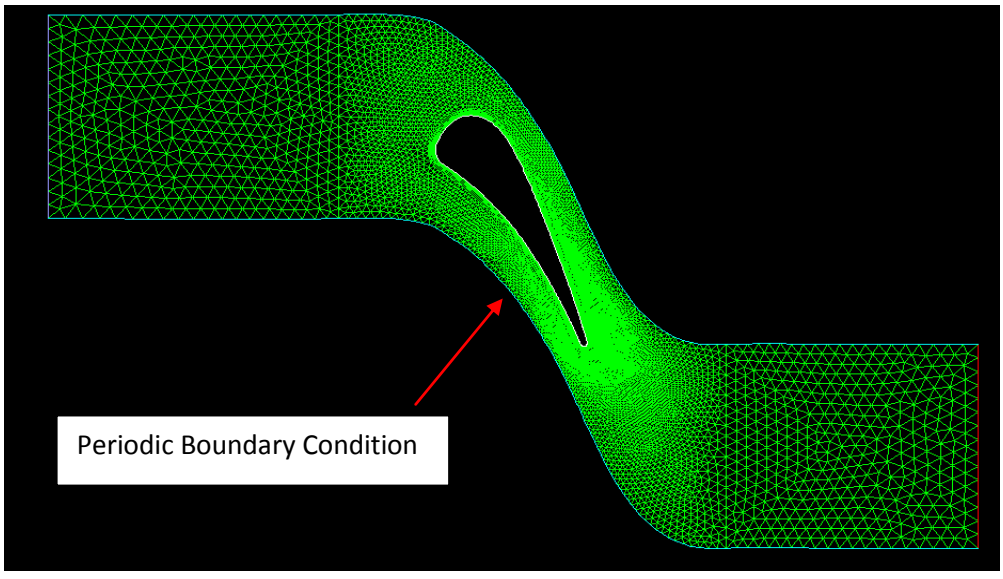

Figure 32: Periodic Boundary Condition in Gas Mesh Used For Local Temperature and Velocity Values

As a result of this change, $\theta = \frac{T_G - T_C}{T_G - T_W(x)}$ was redefined as $\theta = \frac{T_R(x) - T_C}{T_R(x) - T_W(x)}$. The new definition for θ is more appropriate for usage with high speed flow and flows that have work extraction. It also is consistent for any calculation based on data from the empirical film model. The results for T_R calculation are shown in Figure 33. It can be seen that variation in the local gas temperature is as large as 100 K. The recovery factor reduces this variation to 30 K, however local variation is still present.

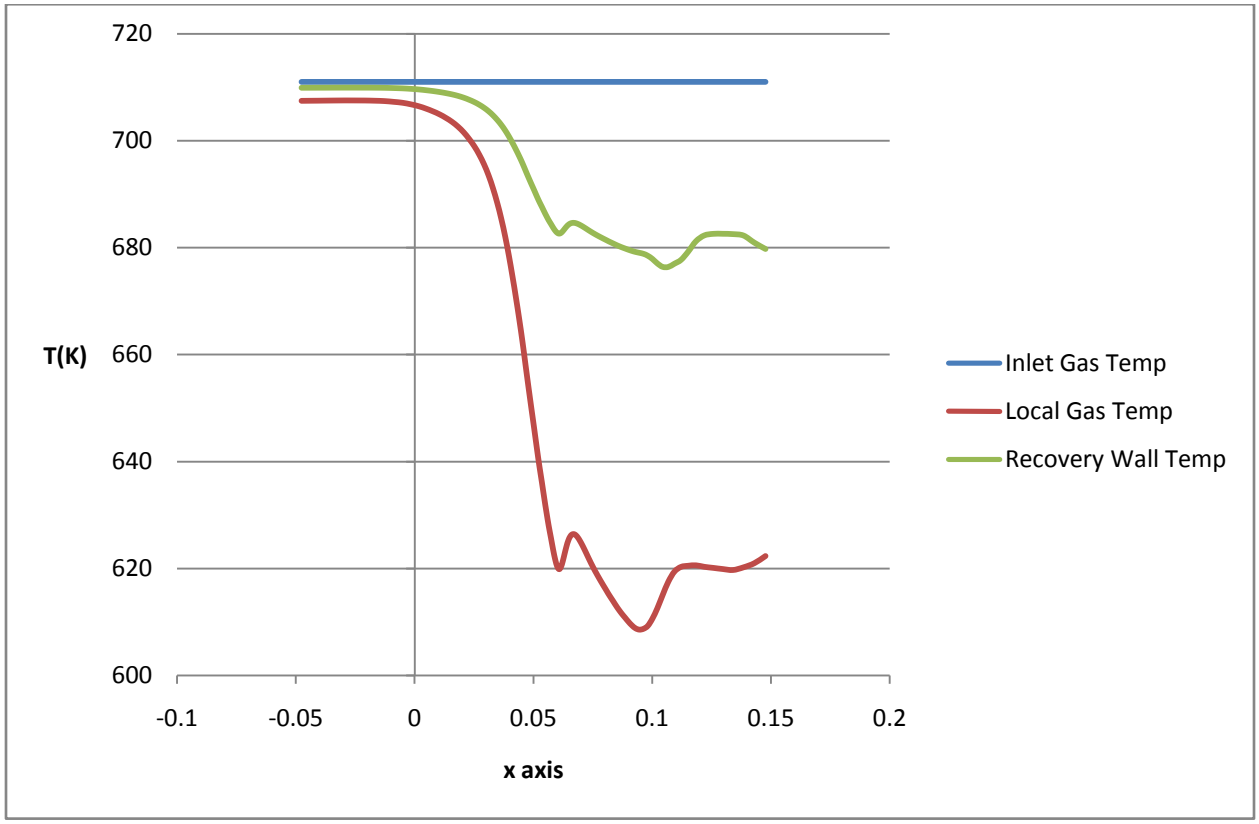

Figure 33: Variation in Inlet Gas Total Temp, Adiabatic Wall Temp and Local Static Temp for Hylton Case

As expected, the predicted wall temperature did not change greatly due to the lack of work extraction, shown in Figure 34. Red lines show the updated wall temperatures based on the new definition of θ. The old values, shown with green and purple lines, fall directly behind the new results. Were this analysis being applied to a blade instead of a vane, the changes in wall temperature would have been significant due to the fact that the flow loses energy. This particular case has no work extraction, so it is expected that the results would be this close.

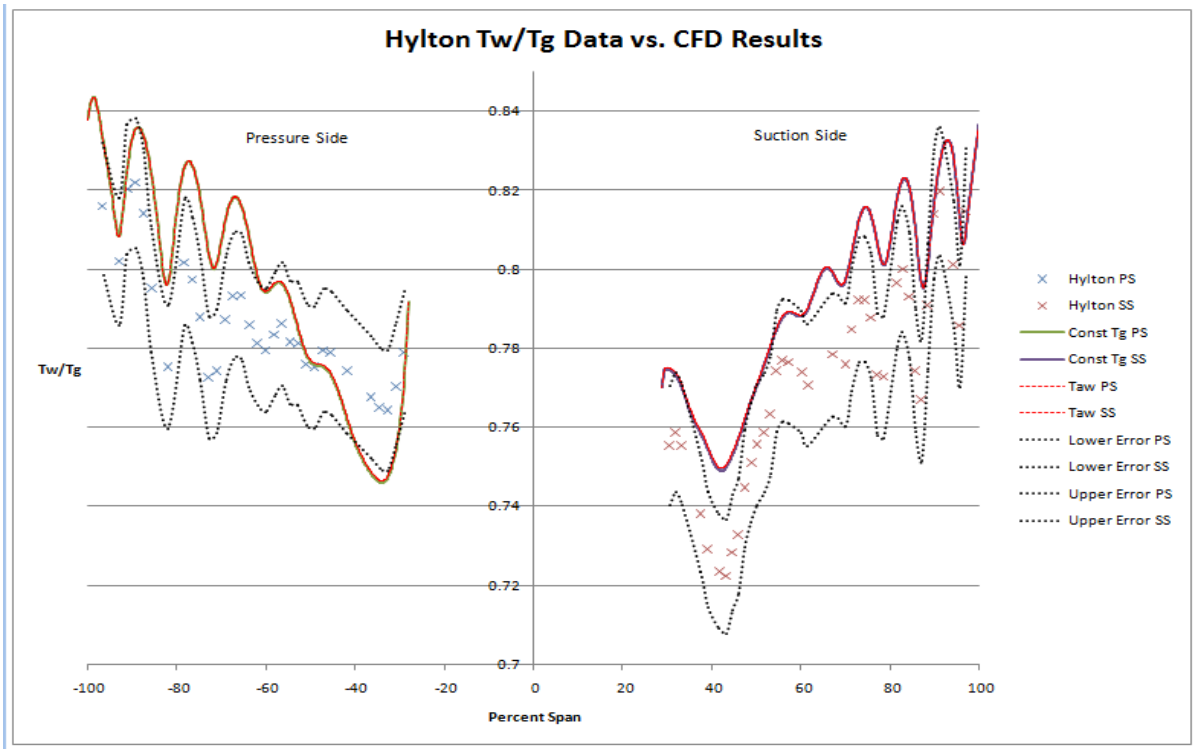

Figure 34: Predicted Wall Temperature Distribution Using Adiabatic Wall Temperature As Reference For Hylton Film-Cooled C3X Vane Solution

5.2 Use of Surface Distribution of η and h_f/h_o for Three-Dimensional Blade Temperature Calculations

Updating the film-cooling script to handle two-dimensional input instead of one-dimensional input greatly enhances the method's capabilities. In this case, ROFM uses surface contour data, from either experiments or film-cooling models. Utilizing two-dimensional data allows ROFM to modify heat transfer coefficients as a surface corresponding to a three-dimensional model, instead of a line corresponding to a two-dimensional model. Further, two-dimensional data allows for capturing more complex phenomena such as second order convective effects that are lost when data is averaged. Figure 35 shows experimental results reported by Yuen et al. [10-13] for local heat transfer augmentation and film effectiveness downstream of three cooling holes. The lateral variation, especially in the near field, was a driving factor in pursuing the capability of using data sets such as this. With one dimensional correlations, the near field data would be span wise averaged, and local variations would be lost entirely.

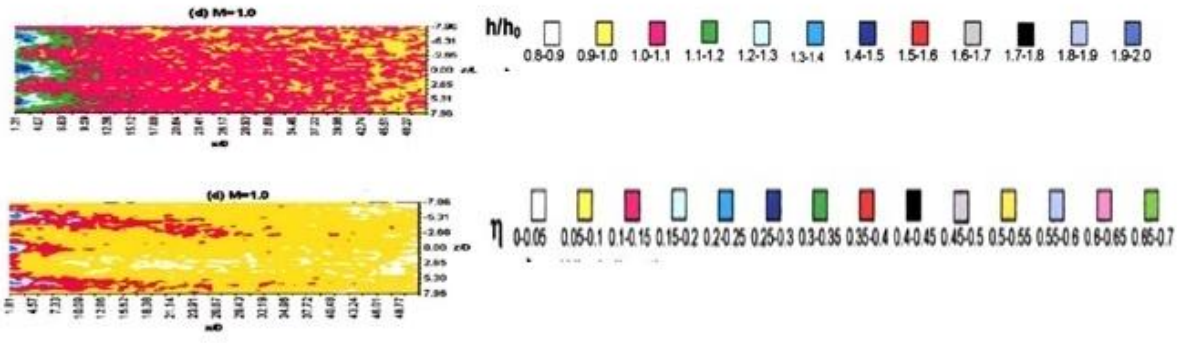

Figure 35: Yuen Film Effectiveness and HT Augmentation Contours [10-13]

5.3 Application of ROFM to Full Coverage Region

The main difference between a code capable of modeling full coverage film-cooling and one that is not is the capability to account for the near field. Modeling the near field requires having a data origin at the start of the cooling hole, shown in Figure 36.

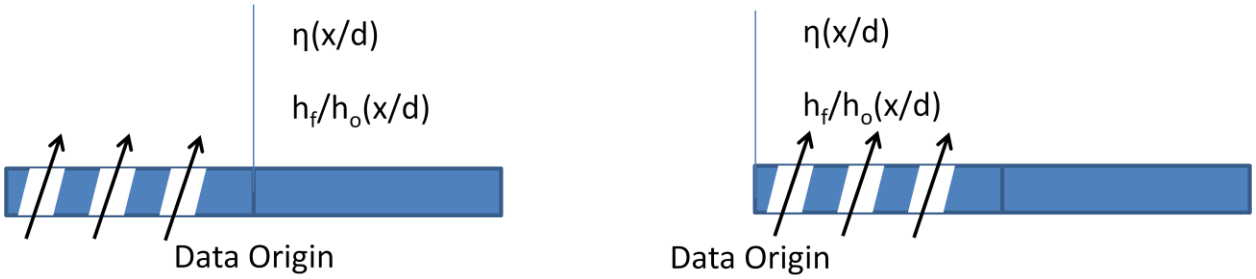

Figure 36: Diagram Depicting Change in Origin Change for Full Coverage Film-Cooling

Changing ROFM to be capable of solving in the full coverage region requires modifying the Scheme code and meshes. The meshes have to be altered to add distinct regions in the place of film-cooling holes. These regions require a temperature boundary condition based on an approximation of the local coolant temperature. The Scheme code is changed to apply additional convective boundary conditions to model heat transfer in the cooling holes prior to injection, shown in Figure 37, and replacing the metal temperature with a constant value equal to the coolant temperature at the injection site.

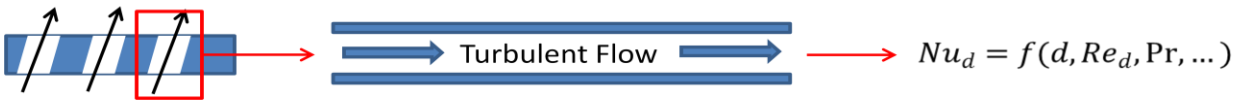

Figure 37: Use of Pipe Flow Nusselt Number Correlations with Full Coverage Film Cooling

These modifications are necessary for ROFM to be used for analyzing blades and vanes in a gas turbine engine. In more demanding engine designs, the entire first stage vane is covered by film-cooling, and as technology continues to evolve this could become the case for other airfoils in the engine. As gas temperatures continue to increase in designs, film-cooling will spread to cover increasingly larger amounts of the surface area, necessitating the ability to solve for accurate wall temperatures near injection sites.

Chapter 6: Summary and Conclusions

The Reduced-Order Film Model was used in conjunction with an empirical film-cooling model provided by Pratt & Whitney to predict wall temperatures of a C3X vane using Fluent. The film-cooling model was used to provide film-cooling effectiveness and heat transfer augmentation values for the geometry and flow conditions reported in Hylton et al. [16-17]. Once these values were obtained, a systematic approach to modeling the Hylton test case was employed. The pressure distribution obtained from the gas solution was compared to reported values and was found to be in good agreement with the Hylton pressure distribution data set [17] as well as Leylek's computational pressure distribution [25] for the same problem.

After matching the pressure distribution, the non-film-cooled case was ran. Wall temperatures were found to match very well with Hylton's experimental data, with the largest deviation being 2.4%. The boundary conditions determined for use on the non-film-cooled case were modified and applied to the film-cooled case. The predicted wall temperature distribution showed a maximum deviation of 3.33%. Given that the experimental error for the wall temperature measurements were $\pm$2%, without calculating any additional error associated with the film-cooling parameters generated with the empirical film model, the results are promising. Further, conjugate heat transfer effects were shown to be significant in the solution, causing local temperature variations as large as 5.6% of the inlet total gas temperature. This value corresponds to a 40°C difference which is quite significant in gas turbine design. Such promising results show that ROFM is capable of accurately solving film-cooled flows and implies that the underlying assumption in ROFM is accurate.

ICHT was expanded to manipulated two-dimensional data, allowing for it to be used for solving for a three-dimensional temperature distributions. ROFM was modified to use a local gas temperature as a reference for calculating film-cooling parameters. The change used the recovery temperature as the reference value in film-cooled flows rather than the inlet total temperature. This is more accurate in instances with work extraction and high speed flow, where the main stream gas temperature varies across the span of the airfoil. ROFM was also extended for use in the near field of a discrete cooling hole. This change allows the method to be used in solving a full coverage film-cooled surface.

Chapter 7: Future Work

Validating ROFM for a three-dimensional case is the most important piece of work that has yet to be done. This is in the process of being completed. Pratt & Whitney will be providing pyrometry data for a V2500 vane. The problem will be solved using Pratt & Whitney's film-cooling correlations to build a surface for film-effectiveness and heat transfer augmentation values. These would then be used to correct the boundary conditions as described herein.

There is currently development on film-cooling and heat transfer augmentation correlations. The correlations calculate span wise decay and lateral spreading values for individual cooling holes. These decay predictions result in two-dimensional film effectiveness predictions that can be turned into a surface. These are than superimposed to generate a single surface. An example for a single hole is shown in Figure 38. These surfaces can be represented as contours for publication or can be handed to ROFM for use in a problem solution. The completion and validation of these correlations increases the value of ROFM as a design tool because it is no longer reliant on a specific experimental data set.

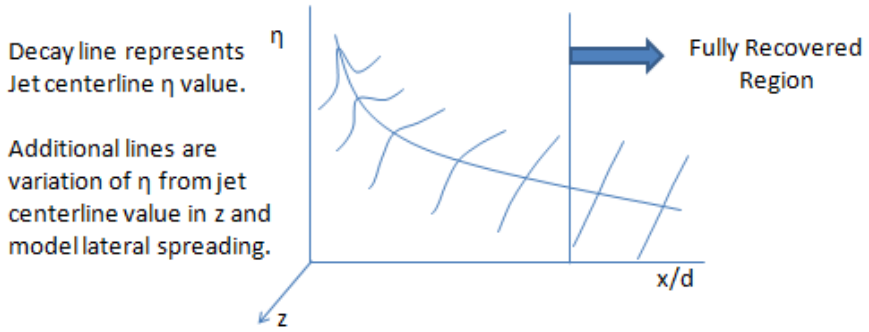

Figure 38: Example of Single Hole Output of Correlations Under Development

A schematic of an experiment, shown in Figure 39, for producing a data set capable of validating the main assumption used in ROFM, that $\left(\frac{h_f}{h_o}\right)_{conj} = \left(\frac{h_f}{h_o}\right)_{non-conj}$, may be conducted. The information required includes film-cooled and non-film-cooled results for conjugate and non-conjugate cases. The left side of Figure 39 shows two flat plate experiments with no film-cooling. The position of the heater, used to provide a constant heat flux, is changed. In the first trial, the heater is above the low conductivity plate, removing conjugate through the metal as a source of resistance to heat transfer. In the second trial, the heater is placed below the low conductivity plate, allowing conjugate effects to be captured. This is repeated with film-cooling added to the experiment. With these results, the assumption could be checked directly by using the experimental data to determine the conjugate and non-conjugate heat transfer augmentation. Currently validation cases have to be used as a source for gauging the accuracy of ROFM. The problem with this is that solving for a correct wall temperature does not prove that the augmentation ratios are equal, it merely implies that it is likely the case. As a result, until this data set is available it is impossible to prove the accuracy of ROFM's underlying assumption.

This experiment would be useful even if it showed that the current assumption is incorrect, but allowed for second order effects to be modeled.

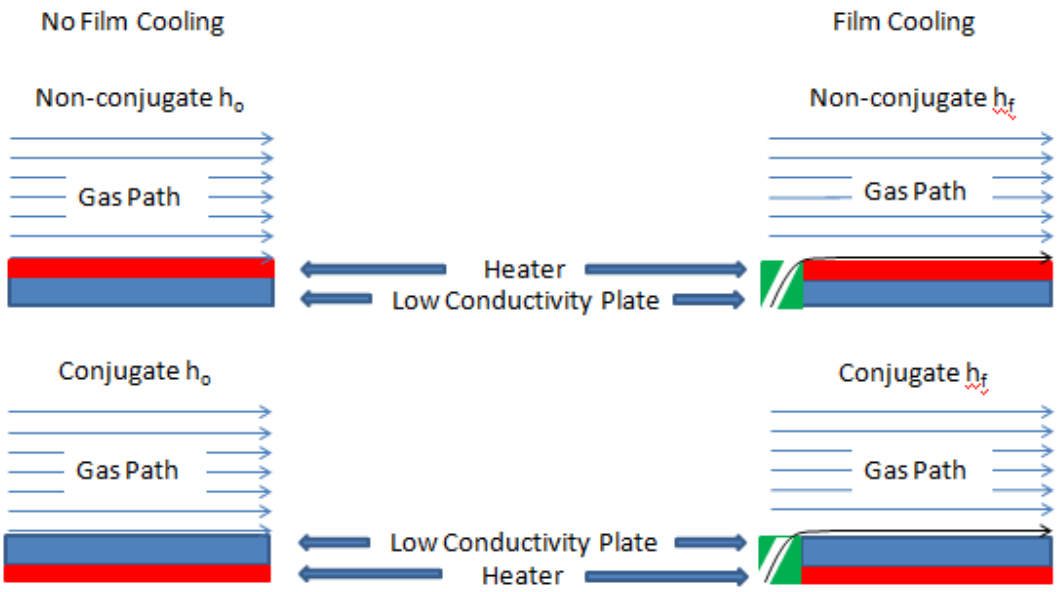

Figure 39: Experiment for Validating ROFM Assumption

Appendix A: Mesh Independence Study

The first mesh generated used more elements, creating a more dense mesh. The grid statistics are provided in Table 4, and a picture of the mesh showing the periodicity is provided in Figure 40. During construction, the grid was divided into three regions. The square region at the inlet contains the front interior line, the front periodic boundary condition and the inlet itself. The square region at the outlet contains the back interior line, the back periodic boundary condition and the outlet. The middle region contains the middle periodic line, as well as the pressure side and suction side of the airfoil. Equiangle and equivolume skew are statistics offered in Fluent for measuring how close the grid elements are to regular shapes. A value of zero would mean every shape is regular, and a value of one refers to highly skewed elements that could result in a solution failing to converge.

Zone	Nodes	Ratio		Boundary Layer		
Inlet	15	1		First Row	1.00E-05	m
Outlet	20	1		Growth Factor	1.1	
Front Interior	40	1		Rows	110	
Back Interior	50	1		Depth	3.574	mm
Front Periodic	30	0.95				
Mid Periodic	250	.98,.98		Equiangle Skew	0.519	
Back Periodic	30	1/0.95		Equivolume Skew	0.35	
Suction Side	328	1/0.996		Wall y+		
Pressure Side	250	0.994		Convergence	3561	iterations
Cells	117183					
Faces	207871					
Nodes	90998					

Table 4: Grid Statistics for Fine Mesh

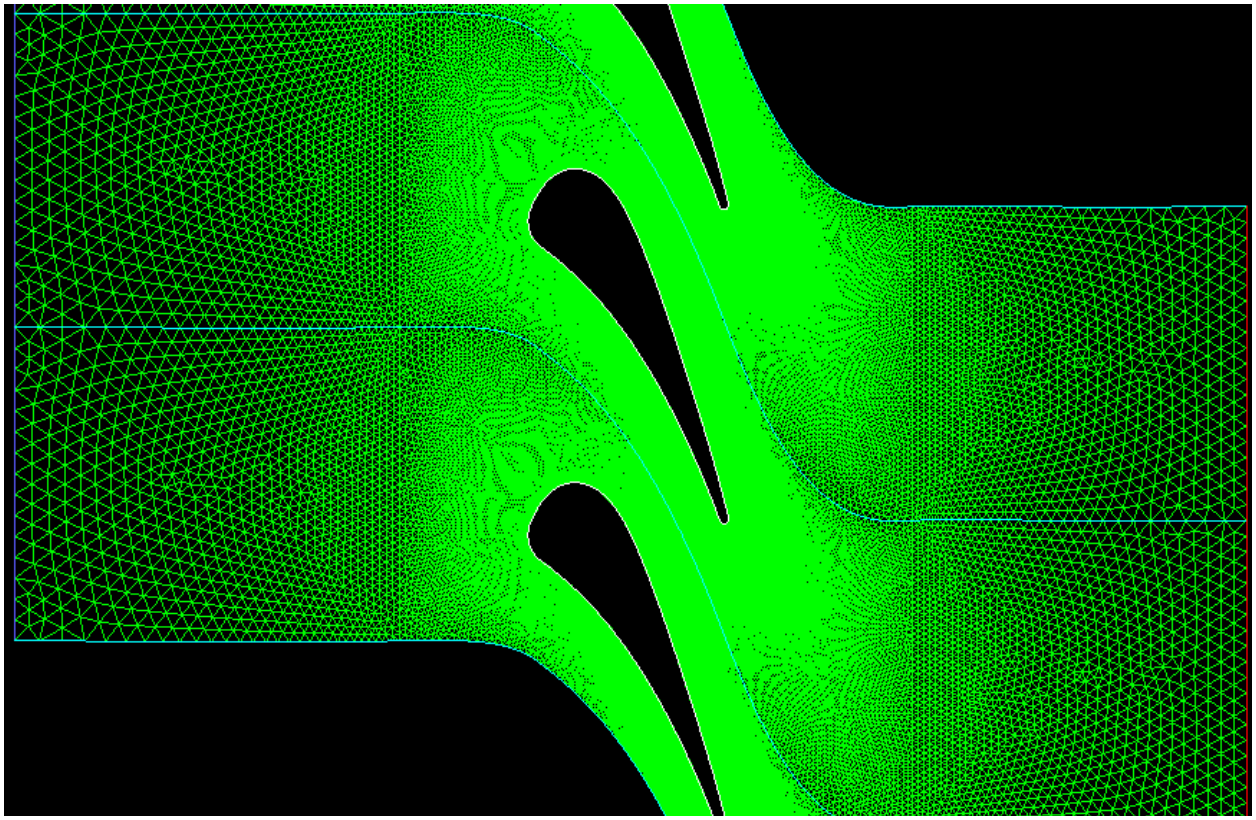

Figure 40: Fine Mesh Showing Periodicity

The second grid generated was much more coarse. The number of faces and nodes was reduced to approximately 33% of the value for the fine mesh. This was done largely in the free stream. The boundary layer mesh density was reduced, but the initial y+ value was held constant. The grid statistics for the coarse mesh can be found in Table 5. Figure 41 shows a picture of the mesh, including the periodicity.

Zone	Nodes	Ratio		Boundary Layer		
Inlet	15	1		First Row	1.00E-05	m
Outlet	15	1		Growth Factor	1.2	
Front Interior	20	1		Rows	62	
Back Interior	20	1		Depth	4.056	mm
Front Periodic	20	0.98				
Mid Periodic	100	.98,.98		Equiangle Skew	0.438	
Back Periodic	20	1/.98		Equivolume Skew	0.302	
Suction Side	192	1/0.99		Wall y+	0.00919	m
Pressure Side	150	0.98		Convergence	1733	iterations
Cells	36222					
Faces	65121					
Nodes	29039					

Table 5: Grid Statistics for the Coarse Mesh

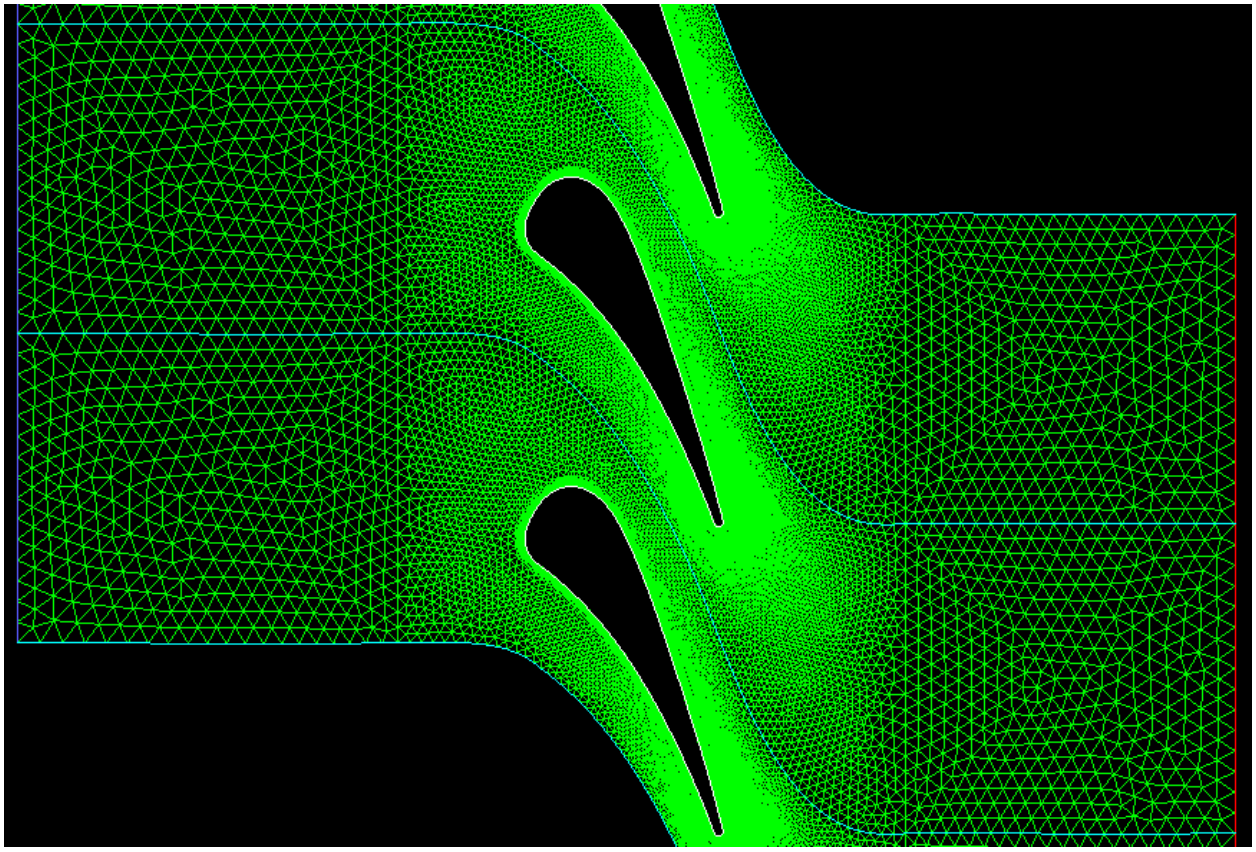

Figure 41: Coarse Mesh Showing Periodicity

Generally phenomena at the wall are used to determine grid independence. In this case, the heat transfer coefficient at the wall was calculated using a second order solution. Figure 42 shows the heat transfer coefficients for the fine mesh while Figure 43 reports values for the coarse mesh. Both meshes reported the same values, concluding that either was sufficient for accurately modeling the problem. The coarse mesh was used for further modeling to achieve quicker run times.

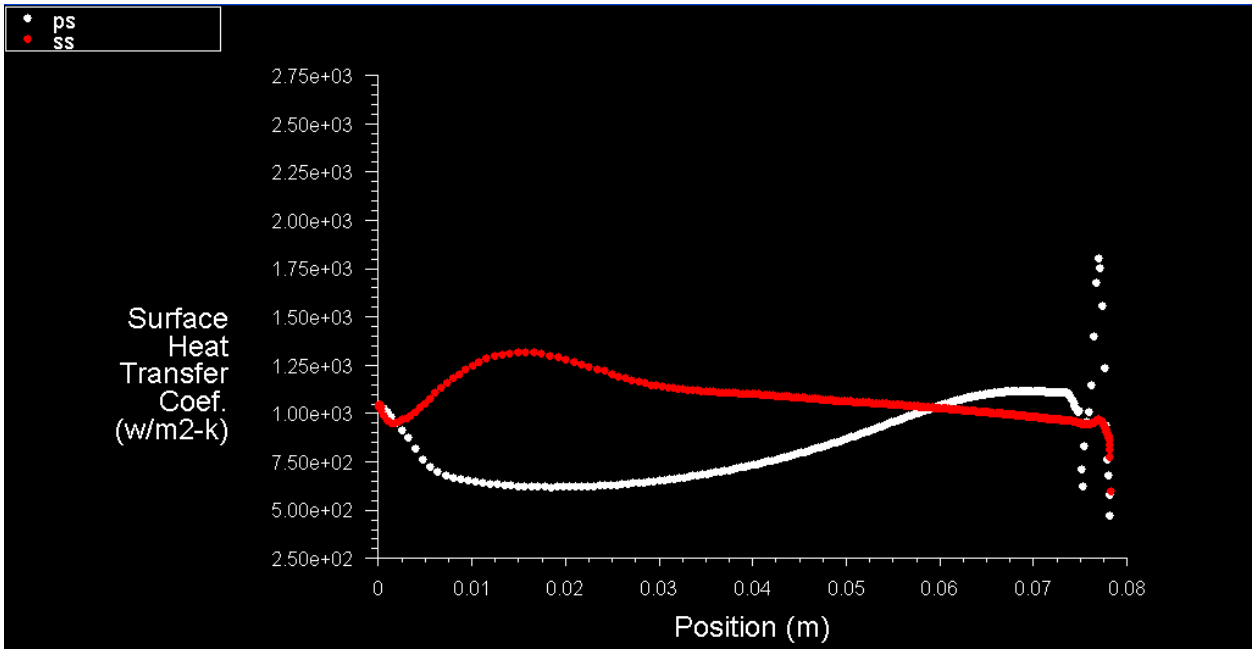

Figure 42: Surface Heat Transfer Coefficient for Second Order Solution Using Fine Mesh

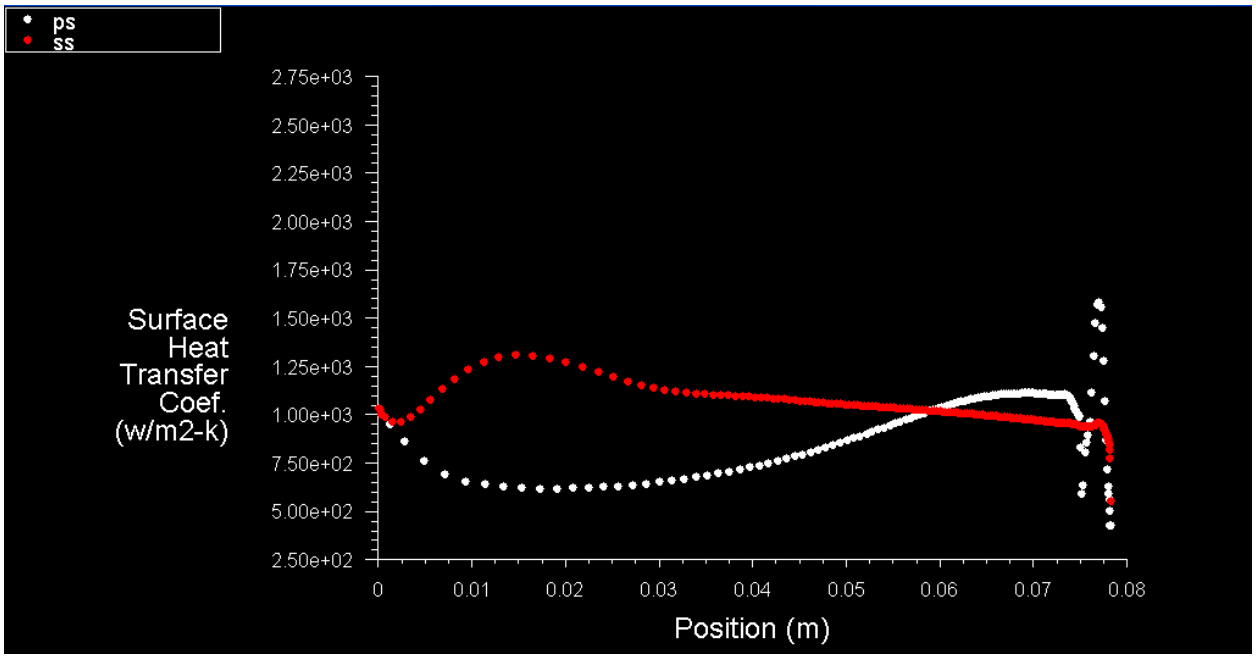

Figure 43: Surface Heat Transfer Coefficient for Second Order Solution Using Coarse Mesh

Appendix B: Information Pertaining to the Hylton et al. [16,17] Experiments

Table 6 provides the vertex data for the C3X vane.

R_{LE} = 1.168 cm (0.460 in.) R_{TE} = 0.173 cm (0.068 in.)

Position number	x--cm (in.)		y--cm (in.)		Position number	x--cm (in.)		y--cm (in.)	
1	0.1097	(0.0432)	11.6548	(4.5885)	40	7.4849	(2.9468)	-0.0617	(-0.0243)
2	0.3894	(0.1533)	12.1890	(4.7988)	41	7.3188	(2.8814)	0.3559	(0.1401)
3	0.7658	(0.3015)	12.6764	(4.9907)	42	7.1483	(2.8143)	0.7737	(0.3046)
4	1.2723	(0.5009)	13.0233	(5.1273)	43	6.9736	(2.7455)	1.1895	(0.4683)
5	1.8743	(0.7379)	13.1376	(5.1723)	44	6.7950	(2.6752)	1.6035	(0.6313)
6	2.4707	(0.9727)	12.9939	(5.1157)	45	6.6116	(2.6030)	2.0155	(0.7935)
7	2.9835	(1.1746)	12.6538	(4.9818)	46	6.4237	(2.5290)	2.4254	(0.9549)
8	3.3985	(1.3380)	12.1976	(4.8022)	47	6.2309	(2.4531)	2.8329	(1.1153)
9	3.7376	(1.4715)	11.6817	(4.5991)	48	6.0328	(2.3751)	3.2380	(1.2748)
10	4.0272	(1.5855)	11.1364	(4.3844)	49	5.8296	(2.2951)	3.6406	(1.4333)
11	4.2885	(1.6884)	10.5766	(4.1640)	50	5.6203	(2.2127)	4.0401	(1.5906)
12	4.5326	(1.7845)	10.0094	(3.9407)	51	5.4051	(2.1280)	4.4364	(1.7466)
13	4.7648	(1.8759)	9.4369	(3.7153)	52	5.1834	(2.0407)	4.8290	(1.9012)
14	4.9870	(1.9634)	8.8605	(3.4884)	53	4.9548	(1.9507)	5.2177	(2.0542)
15	5.2019	(2.0480)	8.2814	(3.2604)	54	4.7191	(1.8579)	5.6020	(2.2055)
16	5.4110	(2.1303)	7.7003	(3.0316)	55	4.4760	(1.7622)	5.9817	(2.3550)
17	5.6157	(2.2109)	7.1176	(2.8022)	56	4.2248	(1.6633)	6.3563	(2.5025)
18	5.8171	(2.2902)	6.5336	(2.5723)	57	3.9654	(1.5612)	6.7249	(2.6476)
19	6.0160	(2.3685)	5.9487	(2.3420)	58	3.6975	(1.4557)	7.0874	(2.7903)
20	6.2126	(2.4459)	5.3632	(2.1115)	59	3.4204	(1.3466)	7.4430	(2.9303)
21	6.4074	(2.5226)	4.7767	(1.8806)	60	3.1339	(1.2338)	7.7909	(3.0673)
22	6.5997	(2.5983)	4.1897	(1.6495)	61	2.8374	(1.1171)	8.1308	(3.2011)
23	6.7894	(2.6730)	3.6015	(1.4179)	62	2.5314	(0.9966)	8.4615	(3.3313)
24	6.9756	(2.7463)	3.0122	(1.1859)	63	2.2149	(0.8720)	8.7826	(3.4577)
25	7.1575	(2.8179)	2.4221	(0.9536)	64	1.8885	(0.7435)	9.0935	(3.5801)
26	7.3335	(2.8872)	1.8301	(0.7205)	65	1.5519	(0.6110)	9.3932	(3.6981)
27	7.5024	(2.9537)	1.2357	(0.4865)	66	1.2052	(0.4745)	9.6815	(3.8116)
28	7.6624	(3.0167)	0.6391	(0.2516)	67	0.8494	(0.3344)	9.9578	(3.9204)
29	7.8115	(3.0754)	0.0411	(0.0162)	68	0.4999	(0.1968)	10.2116	(4.0203)
30	7.8161	(3.0772)	-0.0053	(-0.0021)	69	0.3848	(0.1515)	10.3035	(4.0565)
31	7.8082	(3.0741)	-0.0516	(-0.0203)	70	0.2822	(0.1111)	10.4094	(4.0982)
32	7.7879	(3.0661)	-0.0935	(-0.0368)	71	0.1938	(0.0763)	10.5273	(4.1446)
33	7.7572	(3.0540)	-0.1288	(-0.0507)	72	0.1212	(0.0477)	10.6556	(4.1951)
34	7.7180	(3.0386)	-0.1542	(-0.0607)	73	0.0650	(0.0256)	10.7920	(4.2488)
35	7.6736	(3.0211)	-0.1681	(-0.0662)	74	0.0264	(0.0104)	10.9342	(4.3048)
36	7.6269	(3.0027)	-0.1699	(-0.0669)	75	0.0063	(0.0025)	11.0802	(4.3623)
37	7.5816	(2.9849)	-0.1587	(-0.0625)	76	0.0046	(0.0018)	11.2278	(4.4204)
38	7.5408	(2.9688)	-0.1356	(-0.0534)	77	0.0216	(0.0085)	11.3741	(4.4780)
39	7.5077	(2.9558)	-0.1026	(-0.0404)	78	0.0569	(0.0224)	11.5171	(4.5343)

Table 6: Vertex Data for C3X Vane [16]

Table 7 provides inlet and cooling conditions for the cases ran in the validation study. A subscript of one refers to an inlet value whereas a subscript of two refers to an outlet value.

RUNCODE	PT_1		TT_1		Ma_1	Re_1x10^{-6}	Ma_2	Re_2x10^{-6}	T_W/T_G
	kPa	psia	K	R					
44000	280.35	40.66	709	1277	0.19	0.59	0.89	1.97	0.81
44308	283.93	41.18	711	1280	0.21	0.64	0.89	1.98	0.78
RUNCODE		SUCTION SIDE					LEADING EDGE		
	P_C/P_T	T_C/T_G	COOLANT FLOW RATE			P_C/P_T	T_C/T_G	COOLANT FLOW RATE	
			kg/s	lbm/s				kg/s	lbm/s
44000	1	1	0	0		1	1	0	0
44308	1.614	0.85	0.0234	0.0516		1	1	0	0
RUNCODE		PRESSURE SIDE							
	P_C/P_T	T_C/T_G	COOLANT FLOW RATE						
			kg/s	lbm/s					
44000	1	1	0	0					
44308	1.636	0.85	0.0236	0.052					

Table 7: Inlet and Cooling Conditions for Hylton Cases Used in Validation [16]

Figure 44 provides the normalized pressure distribution for a C3X vane reported by Hylton et al. [17] in 1983. This is the pressure data set used by Leylek [25], Laskowski [26] and this paper for comparison.

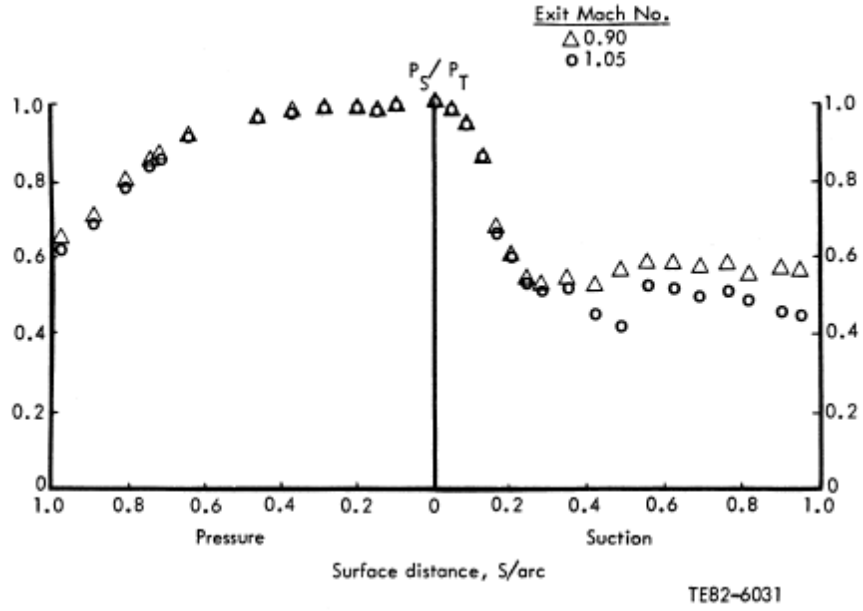

Figure 44: Pressure Distribution for C3X Vane from Hylton 1983 Data Set [17]

Table 8 provides the heat transfer data reported by Hylton et al. [16] for run case 44000. This was the case used for the non-film-cooled analysis.

RUN CODE 44000

SUCTION SURFACE				PRESSURE SURFACE			
% Surface Distance	% Axial Chord	Tw/Tg	h/ho	% Surface Distance	% Axial Chord	Tw/Tg	h/ho
30.57	49.25	.8009	.9518	28.90	34.95	.7749	.6593
31.98	50.84	.7969	.9428	30.78	37.26	.7620	.5766
33.40	52.37	.7907	.9186	32.58	39.43	.7545	.4717
37.60	56.50	.7736	.8219	34.38	41.55	.7554	.4483
39.08	57.92	.7661	.7615	36.29	43.76	.7580	.4059
41.80	60.34	.7596	.6871	41.70	49.81	.7720	.3713
43.25	61.62	.7595	.6895	45.37	53.70	.7818	.3738
44.57	62.74	.7661	.6742	47.14	55.56	.7842	.3914
46.03	63.96	.7700	.6696	49.03	57.47	.7824	.4051
47.51	65.26	.7799	.7406	50.84	59.28	.7852	.4171
48.95	66.44	.7851	.7095	52.68	61.08	.7924	.4526
50.31	67.53	.7893	.6648	54.48	62.81	.7965	.4763
51.78	68.75	.7923	.5978	56.34	64.57	.8033	.5017
53.14	69.77	.7968	.6320	58.12	66.24	.8033	.5461
54.62	71.01	.8067	.7374	59.97	67.92	.8011	.6035
55.97	71.99	.8091	.6512	61.77	69.55	.8046	.6030
57.36	73.07	.8082	.6113	63.63	71.18	.8113	.4959
60.29	75.38	.8083	.6425	65.41	72.73	.8194	.5052
61.67	76.42	.8052	.6247	67.30	74.37	.8211	.4626
67.29	80.63	.8126	.6683	69.07	75.85	.8174	.5102
70.13	82.74	.8125	.7004	70.91	77.38	.8073	.6156
71.51	83.72	.8206	.6491	72.72	78.84	.8063	.6761
73.03	84.92	.8272	.6291	74.63	80.37	.8210	.5563
74.39	85.88	.8275	.5668	76.40	81.77	.8303	.4463
75.74	86.80	.8249	.5878	78.27	83.24	.8349	.4128
77.24	87.96	.8124	.6512	81.91	86.03	.8149	.6423
78.62	88.92	.8127	.6758	85.55	88.71	.8340	.4094
81.54	91.06	.8340	.5112	87.39	90.05	.8512	.3556
82.88	91.94	.8374	.5342	89.25	91.42	.8587	.4699
84.34	92.98	.8331	.5744	91.03	92.66	.8584	.7674
85.70	93.87	.8176	.5625	92.86	93.93	.8438	.8270
87.11	94.82	.8122	.6059	96.55	96.47	.8567	.5305
88.50	95.72	.8329	.4721				
89.92	96.63	.8533	.4392				
91.35	97.57	.8583	.3630				
94.24	99.40	.8448	.6028				
95.65	100.24	.8331	.4791				
97.03	101.02	.8568	.7286				

Table 8: Heat Transfer Data for Non-Film-Cooled Test Case, Run Code 44000 [16]

Table 9 provides the heat transfer data reported by Hylton et al. [16] for run case 44308. This was the case used for the film-cooled analysis.

RUN CODE 44308

SUCTION SURFACE				PRESSURE SURFACE			
% Surface Distance	% Axial Chord	Tw/Tg	h/ho	% Surface Distance	% Axial Chord	Tw/Tg	h/ho
30.57	49.25	.7554	.3954	28.90	34.95	.7790	1.0201
31.98	50.84	.7587	.6844	30.78	37.26	.7703	.9107
33.40	52.37	.7553	.7750	32.58	39.43	.7643	.7721
37.60	56.50	.7382	.7424	34.38	41.55	.7650	.7222
39.08	57.92	.7291	.6852	36.29	43.76	.7677	.6818
41.80	60.34	.7235	.6290	41.70	49.81	.7742	.5593
43.25	61.62	.7223	.6130	45.37	53.70	.7789	.5271
44.57	62.74	.7283	.5882	47.14	55.56	.7795	.5487
46.03	63.96	.7327	.5790	49.03	57.47	.7752	.5632
47.51	65.26	.7447	.6414	50.84	59.28	.7760	.5735
48.95	66.44	.7511	.6147	52.68	61.08	.7813	.6060
50.31	67.53	.7556	.5667	54.48	62.81	.7815	.6062
51.78	68.75	.7588	.5034	56.34	64.57	.7862	.5987
53.14	69.77	.7634	.5267	58.12	66.24	.7834	.6197
54.62	71.01	.7743	.6105	59.97	67.92	.7795	.6781
55.97	71.99	.7770	.5397	61.77	69.55	.7813	.6762
57.36	73.07	.7765	.5063	63.63	71.18	.7860	.5504
60.29	75.38	.7740	.5428	65.41	72.73	.7934	.5629
61.67	76.42	.7707	.5342	67.30	74.37	.7932	.5044
67.29	80.63	.7784	.5833	69.07	75.85	.7873	.5357
70.13	82.74	.7759	.6025	70.91	77.38	.7742	.6357
71.51	83.72	.7848	.5495	72.72	78.84	.7727	.7011
73.03	84.92	.7922	.5356	74.63	80.37	.7880	.5821
74.39	85.88	.7923	.4827	76.40	81.77	.7974	.4697
75.74	86.80	.7877	.4968	78.27	83.24	.8017	.4373
77.24	87.96	.7733	.5585	81.91	86.03	.7753	.6197
78.62	88.92	.7728	.5899	85.55	88.71	.7952	.4114
81.54	91.06	.7965	.4349	87.39	90.05	.8142	.3588
82.88	91.94	.8000	.4572	89.25	91.42	.8219	.4633
84.34	92.98	.7931	.4728	91.03	92.66	.8203	.7268
85.70	93.87	.7744	.4705	92.86	93.93	.8020	.7848
87.11	94.82	.7670	.5148	96.55	96.47	.8160	.5050
88.50	95.72	.7908	.3924				
89.92	96.63	.8140	.3613				
91.35	97.57	.8197	.3055				
94.24	99.40	.8011	.5099				
95.65	100.24	.7858	.3815				
97.03	101.02	.8146	.6279				

Table 9: Heat Transfer Data for Film-Cooled Validation Case, Run Code 44308 [16]

References

[1] Han, J.C., Dutta, S., and Ekkad, S.V., 2000, "Gas Turbine Heat Transfer and Cooling Technology", Taylor & Francis, Inc., New York, ISBN# 1-56032-841-X, 646 pages.

[2] Spakovszky, Z. S. "Thermodynamics and Propulsion." ----. D. Quattrochi. Massachusetts Institute of Technology. 10 Feb. 2011.
<http://web.mit.edu/16.unified/www/FALL/thermodynamics/notes/fig1pratturbcool_web.jpg>

[3] Ligrani, Phil. "Internal Cooling - Surface Heat Transfer Augmentation." Ligrani Professional Website. Phil Ligrani. ---. 10 Feb. 2011.
<http://www.ligrani.com/Research/Groups/internalcooling.html>

[4] R.J.Goldstein, "Advances in Heat Transfer, 1971,"Academic Press, New York, pp. 321–379.

[5] Ekkad, Srinath V.,Ou Shichuan., Rivir, Richard B, October 2004, "A transient infrared thermography method for simultaneous film cooling effectiveness and heat transfer coefficient measurements from a single test ASME J. Turbomach", v 126, n 4, p 597-603.

[6] Baldauf, S., Schulz, A., and Wittig, S., 2002 "Heat Flux Reduction from Film Cooling and Correlation of Heat Transfer Coefficients from Thermographic Measurements at Engine like Conditions".

[7] Baldauf, S., Scheurlen, M., Schulz, A., and Wittig, S., 2002, ''Correlation of Film-Cooling Effectiveness From Thermographic Measurements at Enginelike Conditions,'' GT-2002-30180, ASME J. Turbomach., 124, pp. 686–698

[8] Baldauf, S., Schulz, A., and Wittig, S., 1999, ''High Resolution Measurements of Local Heat Transfer Coefficients From Discrete Hole Film Cooling''. ASME J. Turbomach., 123, pp. 749–757.

[9] Baldauf, S., Schulz, A., and Wittig, S., 1999, ''High-Resolution Measurements of Local Effectiveness From Discrete Hole Film Cooling,'' ASME J. Turbomach., 123, pp. 758–765.

[10] C.H.N. Yuen, R.F., Martinez-Botas, January 2003 "Film cooling characteristics of a single round hole at various angles in a crossflow: Part I. Effectiveness", Int. J. Heat Mass Transfer

[11] C.H.N. Yuen, R.F., Martinez-Botas, January 2003 "Film cooling characteristics of a single round hole at various angles in a crossflow: Part II. Heat transfer coefficients", Int. J. Heat Mass Transfer.

[12] C.H.N. Yuen, R.F., Martinez-Botas, 2005, "Film cooling characteristics of rows of round holes at various angles in a crossflow: Part I. Effectiveness", Int. J. Heat Mass Transfer.

[13] C.H.N. Yuen, R.F. Martinez-Botas., 2005, "Film cooling characteristics of rows of round holes at various streamwise angles in a crossflow: Part II. Heat transfer coefficients", Int. J. Heat Mass Transfer.

[14] Gritsch, M., Schulz, A. Wittig, July 1998, “Adiabatic wall effectiveness measurements of film-cooling holes with expanded exits” ASME J. Turbomach, v 120, n 3, p 549-556,

[15] Gritsch, M., Schulz, A.,Wittig, S, 1998, “Heat transfer coefficient measurements of film-cooling holes with expanded exits”ASME, GT, 1998

[16] Hylton, L.D., Nirmalan, V., Sultanian, B.K. and Kaufman,R.M., 1988, "The effects of leading edge and downstream film cooling on turbine vane heat transfer," NASA CR-182133.

[17] Hylton, L. D., Millec, M. S., Turner, E. R., Nealy, D. A. & York, R. E., 1983, “Analytical and Experimental Evaluation of the Heat Transfer Distribution Over Surface of Turbine Vanes” NASA-Report CR 168015.

[18] Yavuzkurt, Savas., Habte, Melaku., 2008, “Effect of computational grid on performance of two-equation models of turbulence for film cooling applications” ASME Turbo Expo, v 4, PART A, p 133-143, 2008, Proceedings of the ASME Turbo Expo: Power for Land, Sea, and Air.

[19] Azzi, A., Lakehal, D. 2001, “Perspectives in modeling film-cooling of turbine blades by transcending conventional two-equation turbulence models” ASME,HTD, v 369, n 5, p 335-347, 2001, Proceedings of the Heat Transfer Division - Volume 5: Computational, Aerospace and Environmental Heat Transfer

[20] Look, Edward K. "Teardrop film cooled blade." Free Patents Online. James Ryley. 28 March 2011. <http://www.freepatentsonline.com/7008186.html>

[21] Silieti, Mahmood., Divo, Eduardo., Kassab, Alain J. 2004 ,“Numerical investigation of adiabatic and conjugate film cooling effectiveness on a single cylindrical film-cooling hole. ASME, HTD, v 375, n 1, p 333-343, 2004, Proceedings of the ASME Heat Transfer division.

[22] Bohn, Dieter E., Becker, Volker J., Kusterer, Karsten A.,1997, “3-D conjugate flow and heat transfer calculations of a film-cooled turbine guide vane at different operation conditions. Source” ASME, [d]10p.

[23] Dhiman, Sushant and Savas Yavuzkurt, "Film Cooling Calculations With An Iterative Conjugate Heat Transfer Approach Using Empirical Heat Transfer Coefficient Corrections", ASME Turbo Expo, v 4, PARTS A and B, p 1607-1616, 2010, Proceedings of the ASME Turbo Expo: Power for Land, Sea and Air.

[24] Dhiman, Sushant., "Film Cooling Calculations With An Iterative Conjugate Heat Transfer Approach Using Empirical Heat Transfer Coefficient Corrections", MS Thesis, The Pennsylvania State University, State College, Pennsylvania, 2010.

[25] Leylek, James H. and William D. York, “Three-Dimensional Conjugate Heat Transfer Simulation of an Internally-Cooled Gas Turbine Vane.” ASME Turbo Expo 2003.

[26] Laskowski, Gregory M., Ledezma, Gustavo A., Tolpadi, Anil K and Ostrowski, Michael C., 2008,"CFD simulations and conjugate heat transfer anaylsis of a high pressure turbine vane utilizing different cooling configurations", The 12th International Symposium on Transport Phenomena and Dynamics of Rotating Machinery Honolulu, Hawaii, February 17-22, 2008. ISROMAC12-2008-20065.

[27] Luikov, A.V. "Conjugate convective heat transfer problems". Feb 1974 .International Journal of Heat and Mass Transfer, v 17, n 2, p 257-265.

[28] ANSYS Fluent 6.3 Documentation, 2006, Fluent Incorporated, Lebanon, NH.